A variational multiscale framework applied to atmospheric flow over complex environmental terrain

M. Ravensbergen[a], T. Helgedagsrud[b], Y. Bazilevs[c], A. Korobenko[a,*]

[a]*Department of Mechanical and Manufacturing Engineering, University of Calgary, Calgary, AB, T2N 1N4*
[b]*Department of Structural Engineering, Norwegian University of Science and Technology, Richard Birkelands v 1a, Trondheim NO-7491, Norway*
[c]*School of Engineering, Brown University, 184 Hope St., Providence, RI 02912, USA*

Abstract

A residual-based variational multi-scale (VMS) modeling framework is applied to simulate atmospheric flow over complex environmental terrain. This stabilized, multi-scale computational fluid dynamics framework is validated on several test cases for use in determining flow patterns over complex environmental terrain using linear finite elements and quadratic non-uniform rational B-splines (NURBS) discretization. For a Gaussian hill (normally distributed surface), stream-wise velocity is compared to published data showing a good agreement. The second validation case is the Bolund hill, for which experimental field study data exists. Simulation results with NURBS discretization compare well in most regions to the measurements.

Keywords: CFD; Complex Terrain; Finite Elements; VMS; NURBS

1. Introduction

Wind energy is a growing source of electricity generation as the world combats climate change. A major knowledge gap in wind energy is the topic of complex (mountainous or hilly) terrain. In such terrain, the wind speed is highly variable based on location. Accurate, site specific prediction of environmental flow over complex terrain is necessary to predict aerodynamic loading which in turn determines annual energy production and turbine lifespan [9, 46, 107, 159, 162]. Although wind energy is the primary application for this work, accurate prediction of local flow field in complex terrain has numerous other engineering applications such as loading on structures such as buildings, bridges, electrical transmission lines, and antenna towers [37, 43, 47, 162]; natural building ventilation and pedestrian wind comfort [91]; airport, power plant, and industrial project siting [79]; pollutant dispersion [3, 4, 48, 51, 52, 101]; soil erosion for agriculture and forestry [37, 72, 106, 152]; and ship manoeuvring in harbours [35].

Full scale experimental field studies give the most accurate description of the flow to understand the physical phenomenon. Some early experimental campaigns from different areas in Scotland in the late 1970's and early 1980's are Askervein Hill [154], Ailsa Craig Island [72], and Blashaval

*Corresponding author

hill [98]. Bradley [37] looked at flow over Black Mountain, a broad hill with uniform slope in Australia. All these cases studied relatively isolated hills with relatively gentle slopes less than 30 degrees and measured wind speed upstream and behind the feature using fixed anemometers. Taylor et al. [153] review and categorize some of the most important field studies from this era, including those just mentioned. Sampling concentration of a source dispersed from upstream can also provide insight. Lavery et al. [89] examined dispersion around Cinder Cone Butte in Idaho. Later, Ryan et al. [113] examined dispersion of a sample released upstream of Steptoe Butte in Washington state.

Recent field studies include more complex topography. Two coastal examples are Ria de Ferrol in Spain, a narrow harbour surrounded by hills and valleys instrumented with 5 ultrasonic anemometers [35] and the cliffs on the island of Madeira [107]. In the later, the use of a sonic anemometer revealed that some locations under consideration for a wind turbine were in highly turbulent re-circulation regions with reversed flow. The Askervein hill has long been the most commonly used field campaign for model validation. However since Askervein has a generally 2-D geometry and steepness less than 20 degrees, it may not represent a complex enough test case for validation [110]. As an alternative, the Bolund hill experiment [30] [32] was conducted for express purpose of validating complex terrain models. The topography features a 10 m high cliff facing the incoming wind, resulting in a large region of separated flow which should be difficult for low fidelity modeling techniques to capture. Flow statistics in the Bolund hill experiment are measured at 10 different mast locations by sonic anemometers. Another recent experiments comes from the New European Wind Atlas near Perdigão in Portugal. The terrain consists of two steep parallel ridges about 1.5 km apart, 4 km long, and 500 m tall, and instrumented with over 50 meterological towers up to 100 m in height and several scanning lidars [97].

Although field studies provide the most accurate information, they are expensive and time intensive. A cheaper, faster alternative that can still provide accurate insights into the underlying physical phenomena are wind tunnel experiments. Wind tunnel experiments on idealized geometries are simpler than measuring wind profiles in the field and more data can be collected. One early experiment often used for validation is the RUSHIL case with 3 hills of varying steepness [78]. Britter et al. [38] performed a wind tunnel experiment to examine the physical effects that occur within the boundary layer in the prescene of hills. Gaussian (i.e. normally distributed) surfaces are a common test case for wind tunnel experiments [158]. Another common test case is a terrain with a sinusoidal profile in the stream-wise direction such as the experiment of Gong et al. [56] where turbulent boundary layer flow is measured on slopes up to 0.5 for two different surface roughness values. Ayotte and Hughes [7] later measured flow over a single sinusoidal ridge with varying surface roughnesses and slopes. Wind tunnel experiments have also been performed on scale models of real topography such as the Askervein hill [156] and Bolund hill [45].

While on-site wind measurements can be more accurate, numerical models are frequently used. Modeling can supplement experiments by filling gaps between measurement locations, allow investigation into effects of changing parameters, and greatly reduce the cost and time requirement to evaluate a location. Both measurement campaigns in real topography and idealized surfaces in wind tunnels are useful for validating models for flow over complex terrain. Early computational models were based on linearized equations of motion. Field experiments of isolated hill with shallow slopes (e.g. [37, 72, 98, 154]) helped to validate the analytical linear theories such as the one introduced by Jackson and Hunt [71]. The model of Jackson and Hunt separates the flow into an inner layer, where local shear stress perturbations from the terrain are significant, and an outer layer where they are not. The model solves a linearized form of the governing Navier-Stokes equations, and has formed the basis for many subsequent linear flow models. Such linear models perform better for terrains with gentle slopes (less than 0.2 [6]), with the linearization of the governing equations contributing to error on stepper terrain [36, 39, 55, 107].

Fully non-linear, 3D, computational fluid dynamics (CFD) has potential to accurately model more complex terrain with steep slopes and sharp angles [31, 35, 55, 111] as it is capable of including effects such as flow separation through the non-linear terms. CFD on complex terrain began primarily with Reynolds Averaged Navier-Stokes (RANS) solvers. Early examples of RANS solvers being used for complex terrain cases include Hewer [61] who modeled flow over the Blashaval hill, Kim et al. [79] who compared different RANS models for the Cooper's ridge, Kettles hill, Askervein hill, and Sirhowy valley cases, and Castro et al. [40] who simulated the Askervein hill case. These RANS models are typically compared with results of linear flow theory models and in general researchers found that their RANS computations were better able to predict fluid velocities than linear models when comparing both models to measured velocities. RANS has also been applied to the kind of idealized geometry that is often tested in wind tunnel experiments, such as a Gaussian hill [96, 109, 177], the geometry from the RUSHIL experiment [42, 50], and a sinusoidal hill [115]. More recently steady state RANS solvers have been applied to large, more complex domains, often with reasonable results except locally in areas with large flow separation or re-circulation bubbles (see e.g. [35, 41, 55, 107, 108, 110, 111]). Blocken et al. [35] simulated the Ria de Ferrol, Spain experiment using 3D steady RANS with $k-\epsilon$ model and obtained the simulation results deviating by 10–20% from measurements depending on grid quality, resolution and surface roughness parametrisation.

Large eddy simulation (LES) is fundamentally superior to RANS in its ability to capture the non-linearities in turbulent flow over highly complex terrain [162]. The increase in fidelity comes with an increased computational cost but recent advances in computing power have made LES solvers more popular for micro-scale studies such as validation against wind tunnel experiments. Some examples include the RUSHIL case [78] which was modeled using LES by Chaudhari [42] and the sinusoidal hill experiment of Gong et al. [56] which was simulated to investigate various sub-grid scale turbulence models and stratified flow models [44, 121, 160]. Flow over a Gaussian hill was modeled with by LES by Kirkil et al. [80]. The Askervein hill case has also been considered using LES [155] and hybrid RANS/LES techniques [116]. Until recently, 3D steady RANS remained the main CFD approach for large areas of complex terrain. Blocken et al. [35] attributes this to two reasons, the first being the increased computational cost and the second being the lack of validation studies and best practice guidelines for cases of complex terrain beyond a single isolated hill. Additional challenges for LES were highlighted in the blind model comparison for Bolund hill [31], where several RANS models predicted velocities and turbulence levels closer to the measured values than the LES models. LES is nevertheless becoming more popular and following the blind study Chaudhari [42] used LES to simulate flow over the Bolund hill with relatively good agreement compared to other modelers attempts. Recently, LES has been successfully applied to larger areas of complex terrain as well, such as the Perdigão region of two parallel ridges [33, 34] and the Sierra Madre wind turbine site [57]. Correctly defining inlet conditions will continue to be a challenge for these very complex regions which do not have a well defined inflow region, but modelers have shown the ability for LES to reproduce at least the main characteristics of the flow even when using periodic boundary conditions [33]. A history of computational modeling for wind energy assessment provided by Ayotte [6] highlights the benefits and drawbacks of linear models, RANS models, and LES.

Accurate LES of complex terrain requires turbulent inflow conditions, which is a challenge that has been address in two main ways, synthetic turbulence generation and precursor simulations. Stevens et al. [118] proposed a 'concurrent' method where data is fed directly into main simulation instead of written to disk. They applied this technique to a wind turbine array. A pressure gradient to drive the flow is applied only in the precursor part of the domain. Munters et al. [100] propose a generalization of the precursor method proposed by Stevens et al. [118] that allows for unsteady mean-flow directions. They find that precursor techniques are preferably to synthetic turbulence generation especially for atmospheric boundary layer (ABL) flow. Baba-Ahmadi and Tabor [8] propose and present multiple methods to drive the flow for precursor simulations, based on mapping velocities from a downstream plane of the simulation back to the inlet. They propose to either make corrections to the mapped velocity, such as one to keep the flow rate constant, or introduce a body force to drive the flow while using periodic boundary conditions in the stream-wise direction. This last method was used for a turbulent channel flow precursor simulation by Helgedagsrud et al. [60] with driving pressure gradient and periodic boundary conditions in the stream-wise direction to simulate fluid structure interaction of buffeting on a bridge section. Tabor and Baba-Ahmadi [122] review treatment of inlet conditions for LES simulations including precursor simulations and synthetic turbulence generation. Lund et al. [95] and Ferrante and Elghobashi

[53] used a ‘recycling’ method where outflow velocity is fed back to the inflow after making adjustments such as keeping flow rate constant. Li et al. [91] looked at the effect that different inflow conditions have and found that using a pre-simulation of the upstream region gave significantly different results than using an empirical logarithmic law velocity profile.

Any LES simulation requires the choice of an appropriate sub-grid scale (SGS) turbulence model and associated constants, to determine parameters such as the eddy viscosity. This eddy viscosity is an ad hoc term with no associated physical property. The variational multi-scale (VMS) residual based concepts for LES [12] do not rely on any ad hoc viscosity terms. The main idea of the VMS formulation, proposed by Hughes et al. [69] and refined in Hughes et al. [70] and Bazilevs et al. [12], is to use variational projections in place of the classical filtered equation approach of LES. Avoidance of filters eliminates the difficulties associated with the use of complex filtered quantities. VMS methods avoid filtering through *a priori* separation of scales. Initially [70] the turbulent eddy viscosity models were used in the small scale equations, in order to have a discrete mathematical representation of all scales. The addition of residual based turbulence modeling to VMS was proposed by Bazilevs et al. [12] who gave a theoretical representation of the fine scales in terms of the coarse scale residuals, removing any reliance on *ad-hoc* parameters such as turbulent eddy viscosity. Additional challenge of the standard LES models is the requirement on a very small mesh resolution near the surface (e.g. on the terrain surface). To address this limitation the mesh relaxation techniques near the wall was proposed in [23] which are based on the weakly enforced essential (Dirichlet) boundary condition.

The VMS formulation has been successfully applied to a wide variety of complex engineering problems, including wind turbines [16, 19, 20, 24–26, 29, 62, 63, 81–85, 112, 123, 125, 144, 145, 173], aerodynamics of bridge cross-section [58, 59], fluid mechanics for stratified flows [26, 168–170, 174], hydrokinetic turbines [10, 172, 178], cavitating flows [11], bioinspired aerodynamics and FSI [5, 28, 123, 125, 127–130, 137, 139, 141, 171], hydrodynamics and FSI of a hydraulic arresting gear [161, 163], flow analysis of turbocharger turbines [102–105, 146], ship hydrodynamics with free-surface flow and fluid–object interaction [1, 2], thermo-fluid analysis of ground vehicles and their tires and brakes [86–88, 135, 136, 142, 143], spacecraft aerodynamics [131, 132], ram-air parachutes [147], rotorcrafts [166] and compressible-flow spacecraft parachute aerodynamics [77, 140], patient-specific cardiovascular fluid mechanics and FSI [13–15, 18, 21, 22, 64, 74, 90, 119, 120, 123–126, 133–135, 138, 139, 148–150, 150, 151, 175, 176], biomedical-device FSI [65–67, 75, 76, 92–94, 164, 165, 167].

Most RANS and LES simulations use finite volume discretization, whereas the VMS framework relies traditionally on the finite element method (FEM). An alternative approach is the concept of isogeometric analysis (IGA), proposed in [68]. It has many similarities to the finite element method, but aims to be more geometrically exact and simplify the meshing process by using methods common in Computer Aided Design (CAD). The approach is based on NURBS (Non-Uniform Rational B-Splines) which are commonly used in CAD software and from which a NURBS mesh can be created. A NURBS mesh has significantly different properties to a FEM mesh, but some useful parallels can be drawn between **control points** in NURBS and nodes in FEM and between **knots** in NURBS and elements in FEM. Full definitions of these terms are presented in Section 2.4. The basis functions of a NURBS patch are C^{p-1} continuous across element boundaries where p is the order of the basis functions. Once a coarse NURBS mesh is defined, it can be refined through knot insertion without changing the underlying geometry it represents, enabling more accurate h-refinement. The use of NURBS can eliminate some approximation of the domain to the physical geometry. Many authors working on atmospheric flow over complex terrain describe a procedure of terrain generation that involves creating a NURBS surface (generally using a CAD software package) to represent the terrain. For example, Makridis [96] in his Ph.D. thesis describes creating a surface to represent the Askervein hill using the NURBS based 3-D modeling software Rhino. Rasouli and Hangan [111] describe a similar process of creating a surface model in a NURBS format. The next step generally taken at this point is to discretize this NURBS surface into finite elements or finite volumes. This effectively reduces the order of the curves describing the surface from cubic or quadratic (depending on the order of NURBS used) to linear. As an alternative, the fluid domain can also be discretized into NURBS elements, eliminating the need for such an approximation of the terrain surface. This approach is used in [17] and [19] for 3D fluid-structure interaction (FSI) simulation of a wind turbine rotor at full scale, where NURBS elements are used for both the rotor structure and the fluid. NURBS have been shown to perform well for these types of fluid simulations. For example, Bazilevs et al. [12] found quadratic NURBS performed significantly better (practically matching direct numerical simulation) than linear elements for turbulent channel flow. In this work, in additiona to standard linear FEM we also use NURBS to discretize the domain of complex topography, which we believe represents a novel contribution to flow modeling over complex terrain.

The framework used in this paper does not include effect of thermal stratification, although the Boussinesq approximation has been previously applied to the VMS framework in [174]. We aim to add this capability in future work. The remainder of this paper is organized as follows. Section 2 describes the modeling framework used. Results are presented in Sections 3 and 4. Conclusions are drawn and next steps outlined in Section 5.

2. Modeling framework

The modeling framework is based on the residual based variational multi-scale concept applied to the Navier-Stokes equations for incompressible flows. Bazilevs et al. [12] showed that the sub-grid scale solution variables are driven by the residuals of the large scale problem, allowing the effect of unresolved scales to be modeled only in the equations representing the smallest resolved-scales, and not in the equations for the large scales. Unlike traditional LES models, the formulation completely avoids filtering, instead providing a mathematical basis to replace *ad-hoc* turbulence models.

2.1. Governing equations

The fluid mechanics governing equations are the Navier-Stokes equations for incompressible flows composed of conservation of momentum,

$$\rho\left(\frac{\partial \boldsymbol{u}}{\partial t} + \boldsymbol{u}\cdot\nabla\boldsymbol{u}\right) - \boldsymbol{f} - \nabla\cdot\sigma = 0, \tag{1}$$

and continuity,

$$\nabla\cdot\boldsymbol{u} = 0. \tag{2}$$

In the above equations, ρ is the fluid density, $\boldsymbol{u}$ is the fluid velocity, and $\boldsymbol{f}$ is the fluid body force. The fluid Cauchy stress, $\boldsymbol{\sigma}$, is defined as $-p\mathbf{I} + 2\mu\epsilon(\boldsymbol{u})$, where p is the pressure, $\mathbf{I}$ is the identity tensor, μ is the dynamic viscosity, and $\epsilon(\boldsymbol{u}) = \frac{1}{2}(\nabla\boldsymbol{u} + \nabla\boldsymbol{u}^T)$ is the strain rate tensor.

The weak form of the set of Navier-Stokes equations for incompressible flows on the domain Ω, given the trial function space $\mathcal{S}$ and test function space $\mathcal{V}$ is: find the velocity-pressure pair $\{\boldsymbol{u}, p\} \in \mathcal{S}$ such that for all test functions $\{\boldsymbol{w}, q\} \in \mathcal{V}$,

$$\int_\Omega \boldsymbol{w}\cdot\rho\left(\frac{\partial\boldsymbol{u}}{\partial t} + \boldsymbol{u}\cdot\nabla\boldsymbol{u}\right)\mathrm{d}\Omega + \int_\Omega \varepsilon(\boldsymbol{w}) : \boldsymbol{\sigma}(\boldsymbol{u}, p)\mathrm{d}\Omega + \int_\Omega q\nabla\cdot\boldsymbol{u}\mathrm{d}\Omega = \int_\Omega \boldsymbol{w}\cdot\boldsymbol{f}\mathrm{d}\Omega + \int_{\Gamma_h}\boldsymbol{w}\cdot\boldsymbol{h}\mathrm{d}\Gamma, \tag{3}$$

where $\boldsymbol{h}$ is the traction acting on the Γ_h part of the domain boundary Γ. Notation is from [28].

2.2. Residual based Variational multi-scale framework

Following the VMS methods of Hughes et al. [69, 70] we decompose the solution and test function spaces into coarse and fine scale sub-spaces. The coarse scale refers to that which is resolved by the finite spatial discretization, and the associated spaces and variables are indicated by a superscript h. The fine scales are those which cannot be represented by the finite spatial discretization, and the associated spaces and variables are indicated with a prime symbol ($'$).

Using the residual based variational multi-scale (RBVMS) formulation of Bazilevs et al. [12] we decompose the solution variables as $\boldsymbol{u} = \boldsymbol{u}^h + \boldsymbol{u}'$ and $p = p^h + p'$ while choosing for the test functions to use $\boldsymbol{w} = \boldsymbol{w}^h$ and $q = q^h$. An exact expression for the fine scale velocity and pressure variables can be found [12] by choosing $\boldsymbol{w} = \boldsymbol{w}'$ and $q = q'$ as

$$\boldsymbol{u}' = -\frac{\tau_{\mathrm{SUPS}}}{\rho}\mathbf{r}_{\mathrm{M}}(\boldsymbol{u}^h, p^h) \tag{4}$$

$$p' = -\rho \nu_{\text{LSIC}} r_{\text{C}}(\boldsymbol{u}^h) \tag{5}$$

where the coarse scale residuals of the momentum and continuity equations are given by

$$\mathbf{r}_{\text{M}}(\boldsymbol{u}^h, p^h) = \rho \left(\frac{\partial \boldsymbol{u}^h}{\partial t} + \boldsymbol{u}^h \cdot \nabla \boldsymbol{u}^h \right) - \boldsymbol{f}^h - \nabla \cdot \boldsymbol{\sigma}(\boldsymbol{u}^h, p^h), \quad \text{and} \tag{6}$$

$$r_{\text{C}}(\boldsymbol{u}^h) = \nabla \cdot \boldsymbol{u}^h. \tag{7}$$

After substituting the solution variable decomposition into Eqn. 3, and using Eqns. 4 and 5 for the fine scale solution variables, the resulting RBVMS formulation can be stated as follows: find $\{\boldsymbol{u}^h, p^h\} \in \mathcal{S}^h$, such that $\forall \{\boldsymbol{w}^h, q^h\} \in \mathcal{V}^h$

$$\begin{aligned}
&\int_{\Omega} \boldsymbol{w}^h \cdot \rho \left(\frac{\partial \boldsymbol{u}^h}{\partial t} + \boldsymbol{u}^h \cdot \nabla \boldsymbol{u}^h \right) \mathrm{d}\Omega + \int_{\Omega} \varepsilon\left(\boldsymbol{w}^h\right) : \boldsymbol{\sigma}\left(\boldsymbol{u}^h, p^h\right) \mathrm{d}\Omega + \int_{\Omega} q^h \nabla \cdot \boldsymbol{u}^h \mathrm{d}\Omega \\
&+ \sum_{e=1}^{n_{el}} \int_{\Omega^e} \tau_{\text{SUPS}} \left(\boldsymbol{u}^h \cdot \nabla \boldsymbol{w}^h + \frac{\nabla q^h}{\rho} \right) \cdot \mathbf{r}_{\text{M}}\left(\boldsymbol{u}^h, p^h\right) \mathrm{d}\Omega \\
&+ \sum_{e=1}^{n_{el}} \int_{\Omega^e} \rho \nu_{\text{LSIC}} \nabla \cdot \boldsymbol{w}^h \mathrm{r}_{\text{C}}\left(\boldsymbol{u}^h\right) \mathrm{d}\Omega \\
&- \sum_{e=1}^{n_{el}} \int_{\Omega^e} \tau_{\text{SUPS}} \boldsymbol{w}^h \cdot \left(\mathbf{r}_{\text{M}}\left(\boldsymbol{u}^h, p^h\right) \cdot \nabla \boldsymbol{u}^h \right) \mathrm{d}\Omega \\
&- \sum_{e=1}^{n_{el}} \int_{\Omega^e} \frac{\nabla \boldsymbol{w}^h}{\rho} : \left(\tau_{\text{SUPS}} \mathbf{r}_{\text{M}}\left(\boldsymbol{u}^h, p^h\right) \right) \otimes \left(\tau_{\text{SUPS}} \mathbf{r}_{\text{M}}\left(\boldsymbol{u}^h, p^h\right) \right) \mathrm{d}\Omega \\
&= \int_{\Omega} \boldsymbol{w}^h \cdot \boldsymbol{f} \mathrm{d}\Omega + \int_{\Gamma_h} \boldsymbol{w}^h \cdot \boldsymbol{h} \mathrm{d}\Gamma.
\end{aligned} \tag{8}$$

Here Ω is divided into n_{el} spatial finite element subdomains denoted by Ω^e. The stabilization parameters in Equation 8 are streamline-upwind pressure-stabilizing (SUPS)

$$\tau_{\text{SUPS}} = \left(\frac{4}{\Delta t^2} + \boldsymbol{u}^h \cdot \boldsymbol{G} \boldsymbol{u}^h + C_I \nu^2 \boldsymbol{G} : \boldsymbol{G} \right)^{-1/2}, \tag{9}$$

where C_I is the constant of the element-wise inverse estimate [28], and least-squares on incompressibility constraint (LSIC)

$$\nu_{\text{LSIC}} = \left(\mathrm{tr} \boldsymbol{G} \tau_{\text{SUPS}} \right)^{-1}, \tag{10}$$

where $\mathrm{tr}\boldsymbol{G}$ is the trace of the element metric tensor $\boldsymbol{G}$ [157]. The element metric tensor is defined as:

$$\boldsymbol{G} = \frac{\partial \boldsymbol{\xi}^T}{\partial \boldsymbol{x}} \frac{\partial \boldsymbol{\xi}}{\partial \boldsymbol{x}}. \tag{11}$$

where $\boldsymbol{\xi}$ and $\boldsymbol{x}$ are the parametric and physical coordinates, respectively, in the context of finite element method [73].

2.3. Weakly Enforced Boundary Condition

The mesh relaxation techniques near the wall are based on the weakly enforced essential (Dirichlet) boundary condition which is implemented on the terrain surface [23]. Relatively fine mesh resolution near the surface boundary is required for accurate results if the Dirichlet boundary condition is strongly imposed [26]. The method, introduced in [23] was shown to essentially relax the grid resolution requirement near the wall. Rather than requiring the solution to exactly satisfy the Dirichlet boundary conditions ("strong satisfaction"), additional terms are added to the VMS formulation (Eqn. 8) to enforce the Dirichlet boundary condition weakly as Euler-Lagrange condition. The additional terms needed to employ the weakly-enforced boundary condition for a prescribed velocity $\boldsymbol{g}$ on the Γ_g part of the domain boundary Γ are

$$\begin{aligned}
&-\sum_{b=1}^{n_{eb}} \int_{\Gamma^b \cap \Gamma_g} \boldsymbol{w}^h \cdot \sigma(\boldsymbol{u}^h, p^h)\boldsymbol{n} \mathrm{d}\Gamma \\
&-\sum_{b=1}^{n_{eb}} \int_{\Gamma^b \cap \Gamma_g} \left(2\mu\epsilon(\boldsymbol{w}^h)\boldsymbol{n} + q^h\boldsymbol{n}\right) \cdot \left(\boldsymbol{u}^h - \boldsymbol{g}\right) \mathrm{d}\Gamma \\
&-\sum_{b=1}^{n_{eb}} \int_{\Gamma^b \cap \Gamma_g^-} \boldsymbol{w}^h \cdot \rho \left(\boldsymbol{u}^h \cdot \boldsymbol{n}\right)\left(\boldsymbol{u}^h - \boldsymbol{g}\right) \mathrm{d}\Gamma \\
&+\sum_{b=1}^{n_{eb}} \int_{\Gamma^b \cap \Gamma_g} \tau_{\mathrm{TAN}} \left(\boldsymbol{w}^h - \left(\boldsymbol{w}^h \cdot \boldsymbol{n}\right)\boldsymbol{n}\right) \cdot \left(\left(\boldsymbol{u}^h - \boldsymbol{g}\right) \left(\left(\boldsymbol{u}^h - \boldsymbol{g}\right) \cdot \boldsymbol{n}\right)\boldsymbol{n}\right) \mathrm{d}\Gamma \\
&+\sum_{b=1}^{n_{eb}} \int_{\Gamma^b \cap \Gamma_g} \tau_{\mathrm{NOR}} \left(\boldsymbol{w}^h \cdot \boldsymbol{n}\right)\left(\left(\boldsymbol{u}^h - \boldsymbol{g}\right) \cdot \boldsymbol{n}\right) \mathrm{d}\Gamma,
\end{aligned} \tag{12}$$

where $\boldsymbol{n}$ is the outward normal vector of boundary Γ_g. The boundary penalty parameters in the tangential and normal directions, respectively are τ_{TAN} and τ_{NOR}. The inflow part of the Dirichlet boundary, Γ_g, is $\Gamma_g^- = \left\{\boldsymbol{x} | \boldsymbol{u}^h \cdot \boldsymbol{n} < 0, \forall \boldsymbol{x} \in \Gamma_g\right\}$. Further details including the stabilization parameters can be found in [27].

The additional terms for the weak boundary condition in Eqn. 12 are added to the left-hand side of Eqn. 8.

2.4. Discretization Methods

In the present work comparison is made between linear FEM and quadratic NURBS [68], which are used for special discretization of Eqn. 8. The 2nd order accurate, implicit, generalized$-\alpha$ time integration scheme is employed for time discretization. At each time step, the resulting non-linear system of equations is solved using Newton-Raphson method. At every non-linear iteration, the linear system of equations is solved using generalized minimum residual (GMRES) method [114].

3. Axis-symmetric Gaussian Hill

We simulate the three dimensional, axis-symmetric Gaussian hill (normally distributed surface) given by $z = h \cdot \exp\left(-0.5(r/\sigma)^2\right)$ where r and z are radial and vertical coordinates, respectively, $h = 700\,\mathrm{m}$ is the height of the hill, and $\sigma = L/1.1774$. $L = 1750\,\mathrm{m}$ is the hill length defined as the value of r where $z = h/2$. Values for L and h, are taken from Prospathopoulos and Politis [109] who simulate the same cases tested here using the in-house RANS solver CRES-flow NS, with $k-\omega$ turbulence model. Our computational domain spans 23 km ($33h$) in the stream-wise direction and span-wise directions. These dimensions are found necessary to ensure independence of the solution from wall or outflow effects. The domain height is 5000 m ($7h$). An isometric view of the Gaussian hill is shown in Figures 1.

A logarithmic velocity profile,

$$U = U_{ref}\frac{u_*}{\kappa}\ln\frac{z}{z_0}, \tag{13}$$

is applied at the inlet, where $\kappa = 0.41$ is von-Karmann constant, $z_0 = 2.29 \times 10^{-7}\,\mathrm{m}$ is the roughness length, and $u_* = \frac{\kappa}{\ln \delta/z_0}$ is friction velocity, where $\delta = 500\,\mathrm{m}$ is the chosen atmospheric boundary layer thickness. The reference velocity $U_{ref} = 10.9\,\mathrm{ms}^{-1}$ is chosen such that the velocity at 90 m elevation $U_{90} = 10\,\mathrm{ms}^{-1}$. The no-slip boundary condition is enforced on the terrain surface. Grid convergence analysis is performed using the strongly enforced no-slip boundary condition which is followed by comparison to the weakly enforced no-slip boundary condition. No fluid penetration is allowed on the sides of the domain. The outflow boundary uses the naturally imposed traction free condition.

3.1. Gauss Hill with Linear Finite Elements

The computational domain is discretized into structured, hexahedral elements. The time step of $dt = 1.0\,\mathrm{s}$ is used for $11 \times 10^3\,\mathrm{s}$ before flow quantities are averaged for another $6 \times 10^3\,\mathrm{s}$, corresponding to approximately 63 and 32 advection hill lengths, respectively. This gives the statistically stationary flow behaviour. Three different mesh resolutions are used, referred to as coarse,

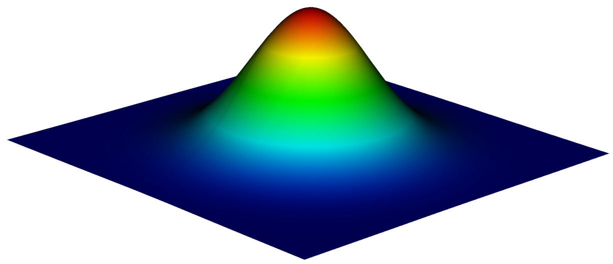

Figure 1: Isometric view of the Gaussian hill. The vertical coordinate is scaled 5x for visibility and the domain is cropped in the horizontal direction with respect to the simulation domain.

medium, and fine. The same time-step is used for all mesh resolutions. The number of elements used in the stream-wise, span-wise, and wall normal directions is show in Table 1. Table 1 also shows the grid convergence index (GCI) based on Richardson extrapolation [54] which is computed for the minimum stream-wise velocity downstream of the hill at 90 m elevation and is less than 5% for coarse to medium and medium to fine meshes. In the stream-wise and span-wise directions the grid is uniformly spaced with the exception of a refinement region between $x \in [-1140, 5700]$ (i.e. $x \in [-1.6h, 8h]$) in the stream-wise direction and $y \in [-684, 684]$ (i.e. $y \in [-h, h]$) in the span-wise direction. In the vertical direction the grid spacing increases with elevation from 6 m ($0.008h$) at the terrain surface to 342 m ($0.5h$) at the upper far field boundary. A cross-section of the computational domain down the centreline along the stream-wise direction for the medium mesh is shown in Figure 2.

Table 1: Mesh Resolution and GCI (FEM)

	Elements	Refinement Ratio	Velocity [m/s]	GCI (%)
Coarse	108x102x25	-	8.43	-
Medium	120x132x50	1.42	8.51	3.2
Fine	144x192x100	1.52	8.65	4.5

Stream-wise velocity 90 m above the terrain surface, for the three different mesh resolutions, is plotted along the length of the domain (x) in Figure 3. All three mesh resolutions show similar maximum velocity over the top of the hill at x=0, with a value about 2% larger than that predicted by Prospathopoulos and Politis [109] (note the non-zero origin on the vertical axis). A slight discrepancy is seen at around the location of the minimum velocity on the downstream side of the hill with the current simulation predicting slightly more slow down in stream-wise velocity.

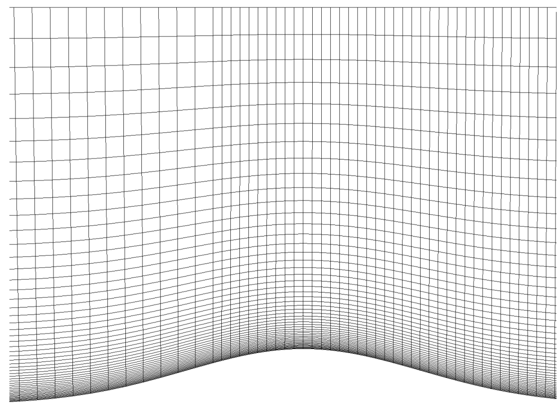

Figure 2: Cross-section of the domain with hexahedral mesh along centreline of Gaussian hill

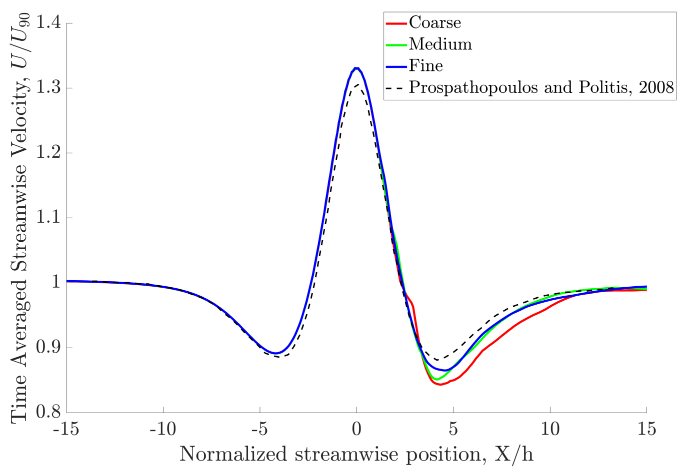

Figure 3: Normalized stream-wise velocity 90 m above Gaussian hill for three grid resolutions with linear FEM

3.2. Gaussian Hill with Quadratic NURBS

We next simulate the Gaussian hill using isogeometric analysis based on NURBS. A NURBS surface is constructed to represent the surface of the Gaussian hill using a NURBS based CAD software. This surface is used as a 'coarse' mesh, and successive refinement is performed without altering the geometry by knot insertion. This process is actually a simplification from the linear finite element approach of the previous section, as for that process the Gaussian hill is initially constructed as a NURBS surface, which is then approximated by bi-linear quadrilateral surface elements during meshing. The same boundary conditions and time-step as described above for the FEM case are used. The number of NURBS elements, defined as knot spans as in Hughes et al. [68], is chosen to be the same as for the finite element meshes.

Stream-wise velocity 90 m above the terrain surface is plotted in Figure 4 for simulations using quadratic NURBS. The maximum velocity predicted by the NURBS simulation for the fine resolu-

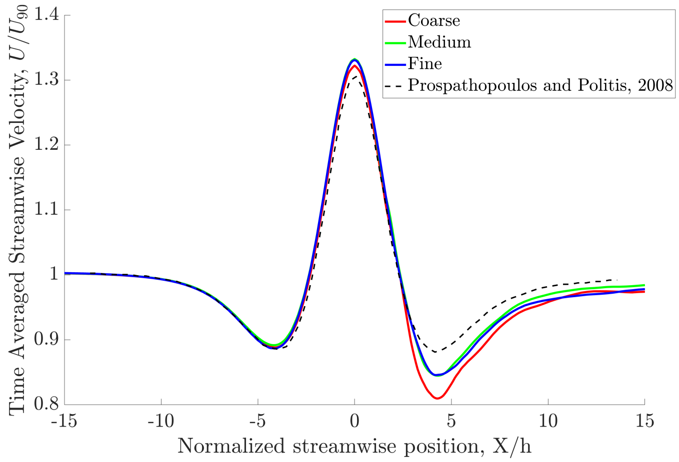

Figure 4: Normalized stream-wise velocity 90 m above Gaussian hill for three grid resolutions with quadratic NURBS

tion is again about 2% higher than the data from Prospathopoulos and Politis [109]. The minimum velocity on the downstream side of the hill is about 4% lower for the fine resolution than the published data. The medium and fine resolutions agree very closely over this region indicating the medium resolution would likely be sufficiently fine in this case. Figure 5 shows an isometric view of the Gaussian surface along with the U component of velocity down the centre of the domain.

The GCI for the minimum velocity behind the hill at 90 m elevation is 0.14% for the coarse to medium mesh and 0.002% for the medium to fine mesh, which, as expected due to the higher order of the shape functions, is much better than the GCI for the linear finite element case.

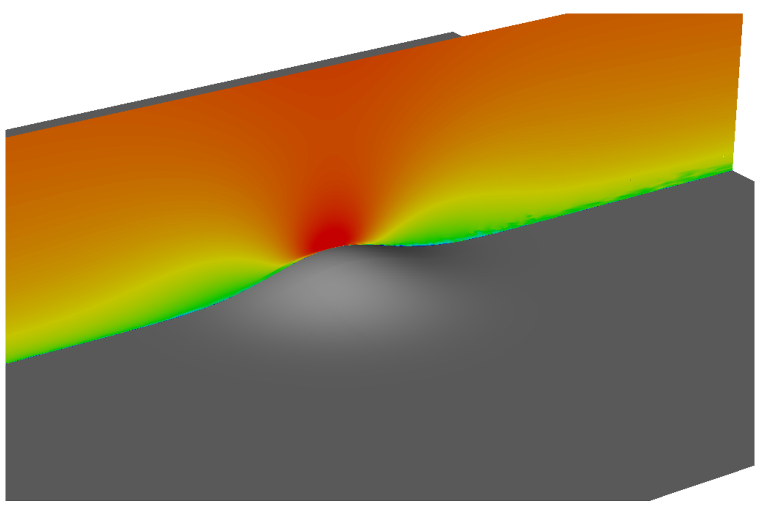

Figure 5: Time averaged stream-wise velocity component for the fine mesh resolution Gaussian hill using NURBS

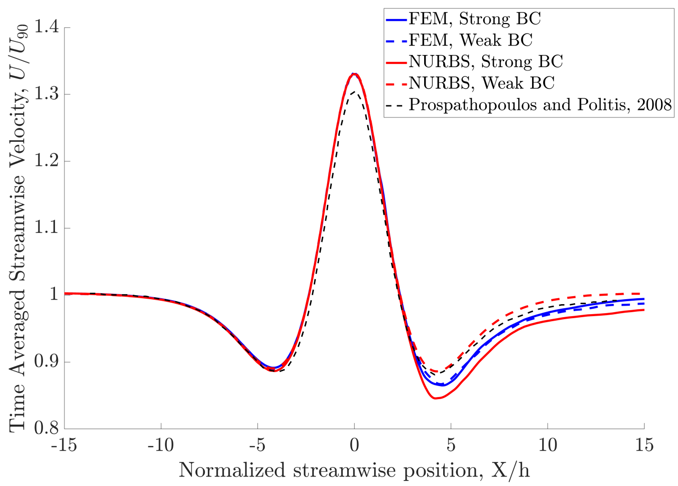

Figure 6: Gaussian hill stream-wise velocity using strong and weak enforcement of the Dirichlet (no-slip) boundary condition. All simulations are for the fine mesh resolution.

3.3. Gaussian Hill with weakly-enforced no-slip boundary condition on the terrain surface

The benefit of employing the weakly-enforced no-slip boundary condition on the terrain surface, as presented in Section 2.3 is investigated next. We compare the usual no-slip boundary condition (strongly enforced) to the weakly-enforced boundary condition for the fine mesh using both FEM and NURBS. The comparison of stream-wise velocity 90 m above the terrain surface is shown in Figure 6 for the fine resolution FEM and NURBS simulations. The simulation using the weak enforcement of the no-slip condition shows less slow down after the hill, more closely matching the published data from [109]. The combination of the relaxation of the no-slip boundary and the higher order of the NURBS basis functions allow the simulation to more accurately capture the flow profile in the re-circulation region, which is dominated by non-linearities.

Comparison of finite element results to the NURBS results is shown in Figure 7 where we compare the medium and fine resolutions using the weakly-enforced boundary condition. The downstream side of the hill again highlights differences in the discretization methods used. The largest slow down is seen with the medium resolution linear FEM simulation. The fine FEM and medium NURBS simulations show fairly similar results, highlighting the increased resolution necessary for FEM given the lower order basis functions. The fine resolution NURBS simulation shows results very similar to the published data with the higher order basis functions better able to capture the sharp velocity gradients in this region.

4. Bolund Hill

The Bolund hill (Figure 8) is a coastal geographical feature in Denmark that was the subject of a field experiment and blind modeling study. The Bolund field campaign provides new dataset for validation of micro-scale LES codes for wind energy applications. This feature is considered a difficult modeling problem due to the nearly vertical escarpment on the upwind side of the hill which produces complex 3-D flow. Data was collected and used to validate models predicting flow in complex terrain [30, 32]. The hill is approximately 12 m high, 130 m long and 75 m wide and is surrounded by water on three sides. The remaining side (on the downstream side for the case considered here) comprises relatively flat terrain. The incoming flow travels over the ocean, making the inflow boundary condition well defined. Measurements are taken at various heights for each of 10 mast locations over 10 min periods, with one mast located far upstream of the hill to quantify the free stream velocity profile and turbulent kinetic energy to provide inflow boundary conditions for simulations. The mast locations are shown in Figure 9. Additionally, limited effects from stratification are expected due to the small hill height relative to boundary layer depth, therefore the approximation of neutral stratification may be considered as valid.

The domain constructed around Bolund hill stretches 390 m across, 800 m long (300 m upstream and downstream of the hill) and 120 m high. This domain size was recommended by Bechmann et al. [31].

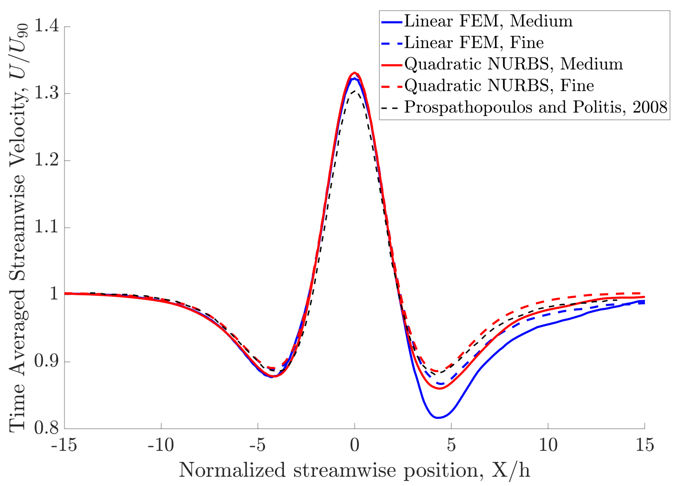

Figure 7: Normalized stream-wise velocity 90 m above the Gaussian hill for linear FEM and quadratic NURBS

Figure 8: Bolund hill (picture from Bechmann et al. [31])

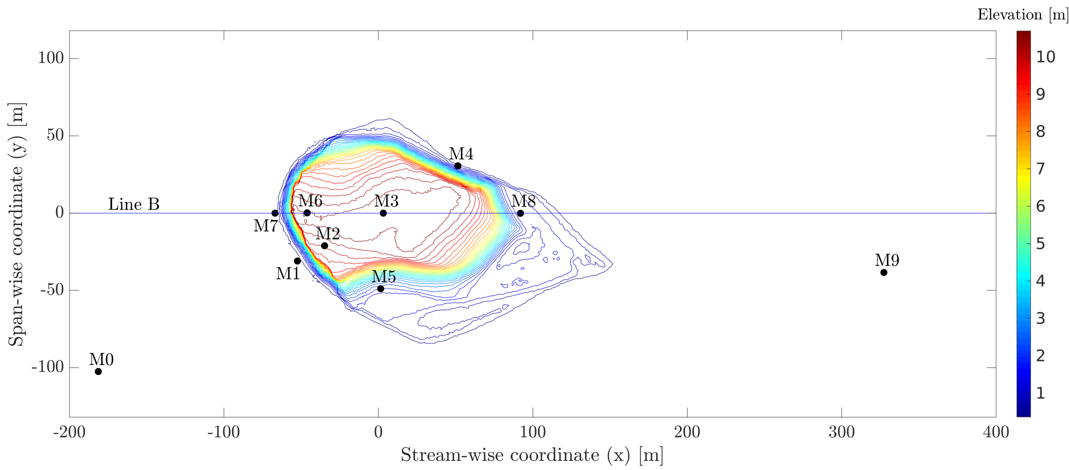

Figure 9: Bolund hill elevation contours and mast locations. Flow is from left to right in the case considered.

4.1. Precursor Simulation

To generate a realistic (turbulent) inflow condition for the Bolund hill simulation, a pressure driven NURBS precursor simulation of flow over a flat plate is used and sequential planes are fed into the main simulation. The method is the same as that described in Helgedagsrud et al. [60] except that we use a half-channel since the no-slip boundary is only on the lower surface of the domain for ABL flow. Periodic boundary conditions are used in the stream-wise and span-wise direction and the no-slip condition is weakly-enforced on the lower boundary. The symmetry condition is employed at the upper boundary. The precursor simulation uses a rectangular domain with span-wise and vertical dimensions equal to those of the main simulation domain (390 m and 120 m respectively). In the stream-wise direction, the domain extends 750 m. 192, 64, and 32 elements are used in the stream-wise, span-wise, and wall-normal directions respectively. The initial condition is a parabolic mean velocity profile based on the bulk velocity with superposed random velocity fluctuations to promote transition to turbulent flow. The flow is driven by a volumetric forcing, f, equal to 3.73×10^{-3} ms^{-2}. The forcing is calculated based on a desired friction velocity Reynolds number, $\mathrm{Re}_\tau = u^* D/\nu = 395$, and bulk velocity, $\overline{U}_b = 11.893$ ms^{-1}. The bulk velocity is the mean velocity based on the suggested logarithmic inflow velocity profile [31],

$$u = \frac{u_0^*}{\kappa} \ln\left(\frac{z_{agl}}{z_0}\right), \tag{14}$$

where (z_{agl}) is the height above the ground, u_0^* =0.4 ms^{-1} is the reference friction velocity measured during the experiment (not to be confused with that used for the precursor simulation), z_0 $=3 \times 10^{-4}$ m is the surface roughness length, and $\kappa = 0.4$ is the von-Karmann constant. The friction velocity and surface roughness are set for 4 different cases in [31] based on fits to experimental data from the upstream mast. The values given refer to case 1 of [31] with 270° flow direction which is the case simulated in this work. The friction velocity Reynolds number is chosen for two reasons. First, similar simulations and experiments performed at this Reynolds number provide data for validation [60, 99]. Secondly, these researchers reported turbulence intensities (TI) of approximately 4.4% for this Re_τ, which is similar to the turbulence level recommended by Bechmann et al. [31], who recommended modellers specify a turbulence kinetic energy value of $TKE = 5.8(u_0^*)^2 = 0.928\,\mathrm{m}^2/\mathrm{s}^2$, constant with elevation. Since both measures of turbulence are based on RMS fluctuations of the diagonal terms of the Reynolds stress tensor, the relation,

$$TI = \frac{\sqrt{\frac{2}{3}TKE}}{\overline{U}_b} = 6.6\%, \tag{15}$$

can be used. With Re_τ and $\overline{U}_b$ determined, the volumetric forcing f can be found by balancing the volumetric forcing with the wall shear force, giving the expression:

$$f = \frac{u^{*2}}{D}, \tag{16}$$

where D is the domain (half-channel) height, and the friction velocity u^* is found through the equation system formed by Spalding's parameterization for the law of the wall [117], Dean's correlation relating the bulk and center line ($\overline{U}_{cl}$) velocities [49], and the definition of Re_τ. The equations

$$\overline{U}_{cl} = u^* g^{-1}(\mathrm{Re}_\tau), \tag{17}$$

$$\overline{U}_{cl} = 1.28\overline{U}_b\left(\frac{2\overline{U}_b D}{\nu}\right)^{-0.0116} = 1.28\overline{U}_b \mathrm{Re}_b^{-0.0116}, \tag{18}$$

$$\nu = \frac{u^* D}{\mathrm{Re}_\tau}, \tag{19}$$

are solved for $\overline{U}_{cl}$, u^*, and ν simultaneously. Re_τ, $\overline{U}_b$ and D are known and g^{-1} is the inverse of Spalding's parameterization,

$$g(u^+) = u^+ + e^{-\chi B}\left(e^{\chi u^+} - 1 - \chi u^+ - \frac{(\chi u^+)^2}{2!} - \frac{(\chi u^+)^3}{3!}\right) \tag{20}$$

where $\chi = 0.4$ and $B = 5.5$.

4.1.1. Precursor simulation results

The simulation is run for 17,000 steps with a time step $dt = 0.2\,\mathrm{s}$, corresponding to the flow travelling over 50 times the domain length. The mean velocity profile was seen to converge to DNS results prior to this point. The simulation was performed on 256 compute cores and take approximately 15 s per time step. Figure 10 shows the domain of the precursor simulation with the periodic and no-penetration boundaries coloured by the instantenous stream-wise velocity component.

Time averaged velocity and turbulence profiles are presented in terms of non-dimensional wall distance (y^+) and velocity (u^+),

$$y^+ = \frac{yu^*}{\nu} = \frac{y\mathrm{Re}_\tau}{D}, \tag{21}$$

$$u^+ = \frac{u}{u^*} = \frac{uD}{\mathrm{Re}_\tau \nu}. \tag{22}$$

Profiles are shown in Figures 11 and 12. Results are very close to published results. DNS data for both is from Moser et al. [99]. The RMS fluctuations are calculated as

$$RMS = \frac{\left(u'^2 + v'^2 + w'^2\right)^{1/2}}{u^*}, \tag{23}$$

where $u' = u - \bar{u}$, $v' = v - \bar{v}$, and $w' = w - \bar{w}$ are the stream-wise, span-wise and wall-normal fluctuating components, respectively.

Comparing the results of the pressure driven, periodic, half-channel precursor simulation with the inflow boundary conditions suggested by Bechmann et al. [31] (Figure 13), there is slight deviation in the mean velocity profile from the log-law profile recommended, but generally good overall agreement. The recommendation of setting turbulence kinetic energy to a constant value

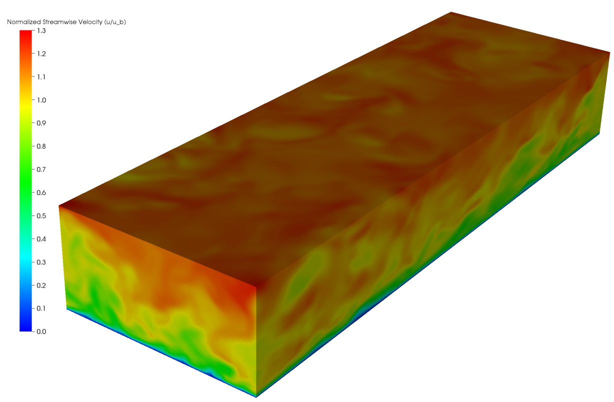

Figure 10: Instantaneous stream-wise velocity component normalized by the bulk velocity for the precursor simulation. The no slip wall is on the bottom (out of sight).

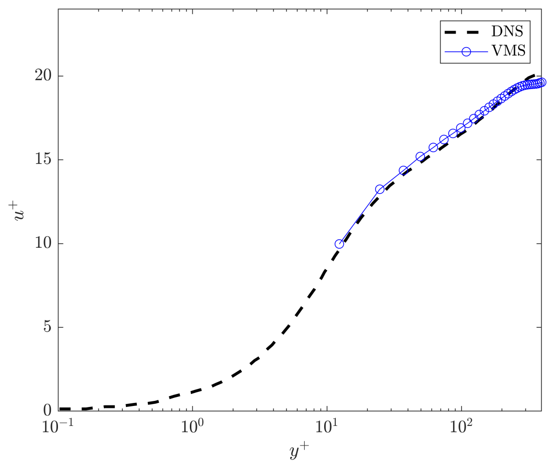

Figure 11: Mean steam-wise velocity of precursor simulation with distance from wall in non-dimensional units. DNS data from Moser et al. [99].

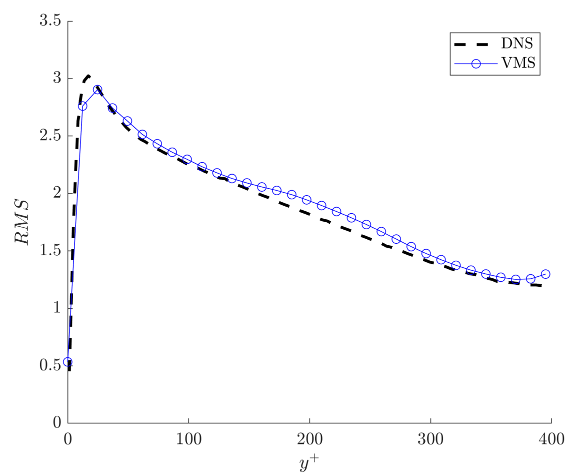

Figure 12: Root mean square of velocity fluctuations ($(u'^2 + v'^2 + w'^2)^{1/2}/u^*$) of precursor simulation with distance from wall in non-dimensional units. DNS data from Moser et al. [99].

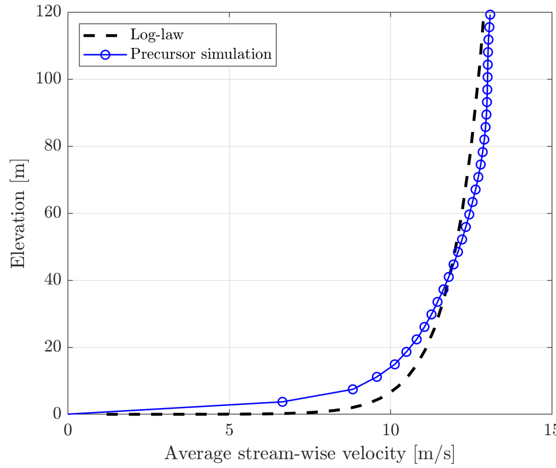

Figure 13: Time averaged stream-wise velocity profile compared with log-law profile proposed at inlet condition by Bechmann et al. [31].

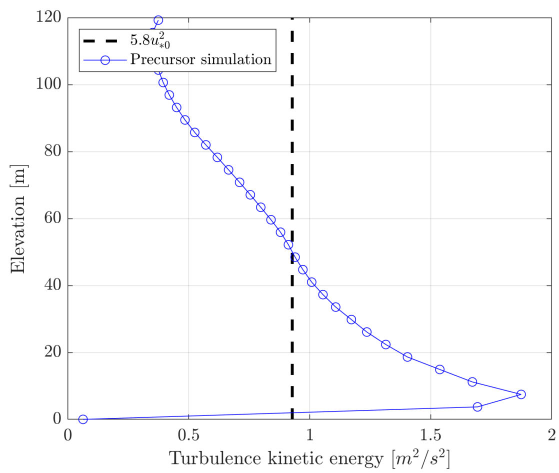

Figure 14: Turbulence kinetic energy ($(u'^2 + v'^2 + w'^2)/2$) profile compared with constant value proposed as inlet condition by Bechmann et al. [31].

with elevation is not physical and does not agree with the result of the precursor simulation (Figure 14), but the value is in a similar range.

4.1.2. Bolund hill precursor coupling

Data transfer from the precursor simulation to the inflow of the Bolund hill simulation is done using the method described in Helgedagsrud et al. [60] based on weakly enforced boundary conditions for Bolund hill NURBS simulation.

After the simulation reached a statistically stationary flow as described in the results section above, successive (in time) planes of the inflow/outflow precursor boundary are fed into the main Bolund hill simulation. As the precursor and Bolund hill mesh do not match one-to-one at the inlet plane, a coupling method is needed to transfer the data. The velocities from the precursor simulation are output (written to disk) at the locations of the integration points of the main simulation. These values are read by the main simulation and enforced in a weak sense on the inflow boundary by setting them equal to the inflow boundary velocity $\boldsymbol{g}$ from Equation 12.

4.2. Bolund Hill with quadratic NURBS

The Bolund hill domain is discretized using quadratic NURBS elements. We decided not to use FEM discretization based on the superior performance of NURBS-based simulations for Gaussian hill in Section 3. To capture the sharp terrain gradient at the upwind side of the hill, the mesh is refined in the stream-wise direction over a distance of 18 m. A cross section of the mesh is shown in Figures 15. Two mesh resolutions are considered, referred to as 'medium' and 'fine'. The fine resolution uses $311 \times 195 \times 82$ elements (4.97 million in total) and the medium resolution uses $275 \times 161 \times 57$ elements (2.52 million in total) in the stream-wise, span-wise, and vertical directions respectively for a horizontal grid spacing of 2 m in the unrefined section for the fine case. The first element in the vertical direction is located at 0.15 m for the fine mesh and 0.5 m for the medium mesh.

The inlet condition at each time step is taken from the precursor simulation, which is run with the same time step as the main simulation. The precursor simulation has the same span-wise and vertical dimensions as the main simulation but different mesh resolution. On the side boundaries no fluid penetration is enforced and the outlet is naturally imposed traction free with a stabilization term to ensure any fluid re-circulation (i.e. negative stream-wise velocity at the outlet) does not result in non-physical effects. On the terrain surface the no-slip boundary condition is enforced weakly. The initial condition is set based on a logarithmic velocity profile with elevation over the entire domain, as in Equation 14.

Figure 16 shows instantaneous stream-wise velocity contours along the $y = 0$ plane for the simulation using NURBS with medium resolution, while Figure 17 show the same quantity time-averaged. Figure 18 shows time averaged velocity streamlines over the upwind slope of the hill. A re-circulation region is seen just behind the edge of the upwind slope.

Results of the simulations are compared to measured data by plotting vertical profiles at each mast location (locations shown in Figure 9). Profiles of velocity magnitude, S, are compared with data points showing measured values in Figures 19 and 20. Results are non-dimensionalized by the reference friction velocity, $u_0^* = 0.4\,\mathrm{ms}^{-1}$, from Equation 14. The simulation using quadratic NURBS elements with medium mesh resolution match the experimental data quite well. The location of specific masts can provide insight into the aspects of the flow that are best captured by the simulation. Masts 1 and 7 are located just in front of the hill. Masts 2 and 6 are located at the top of hill just behind the steep slope on the upstream side. Masts 4, 5, and 8 are located at the

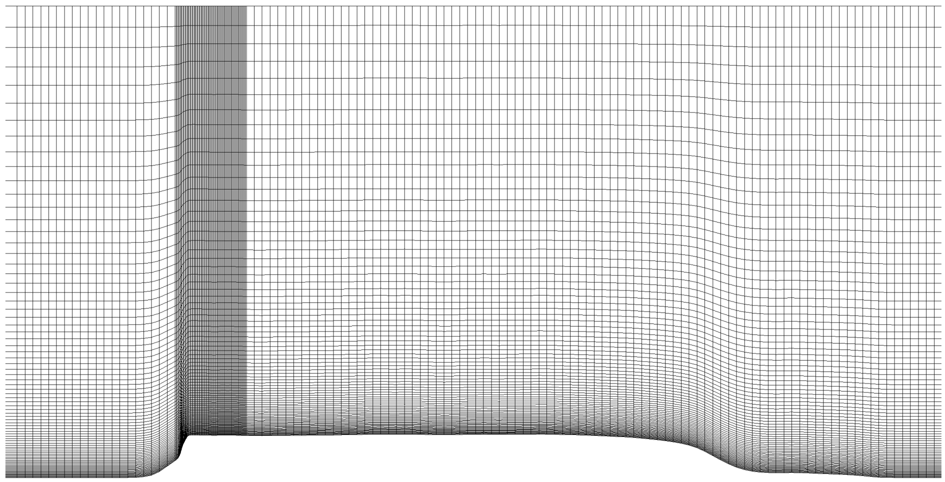

Figure 15: Cross-section of the computational domain for the Bolund hill

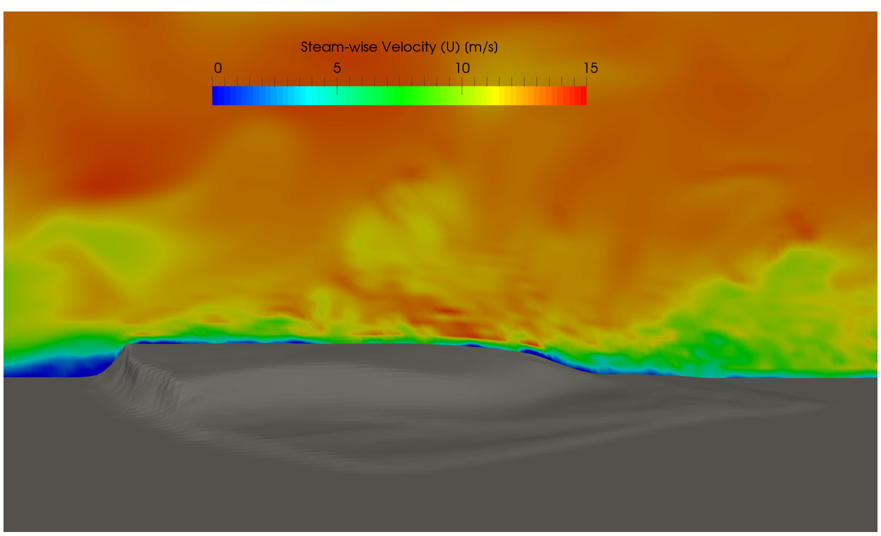

Figure 16: Cross-section of the instantaneous stream-wise velocity component for a medium mesh resolution.

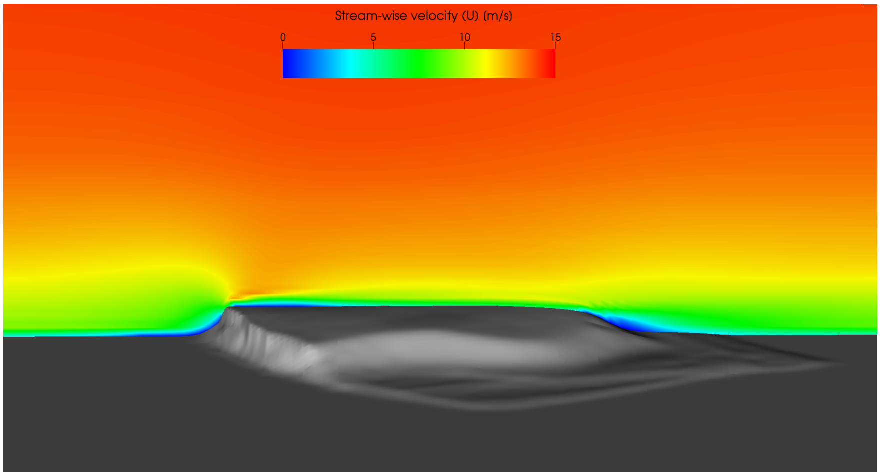

Figure 17: Cross-section of the time averaged stream-wise velocity component for a medium mesh resolution.

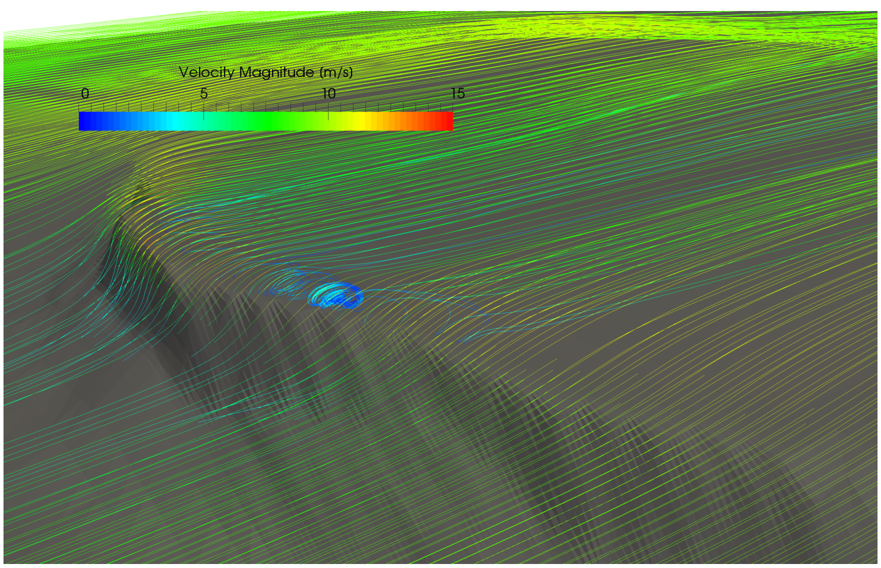

Figure 18: Time averaged velocity streamlines coloured by velocity magnitude for the NURBS simulation with fine resolution

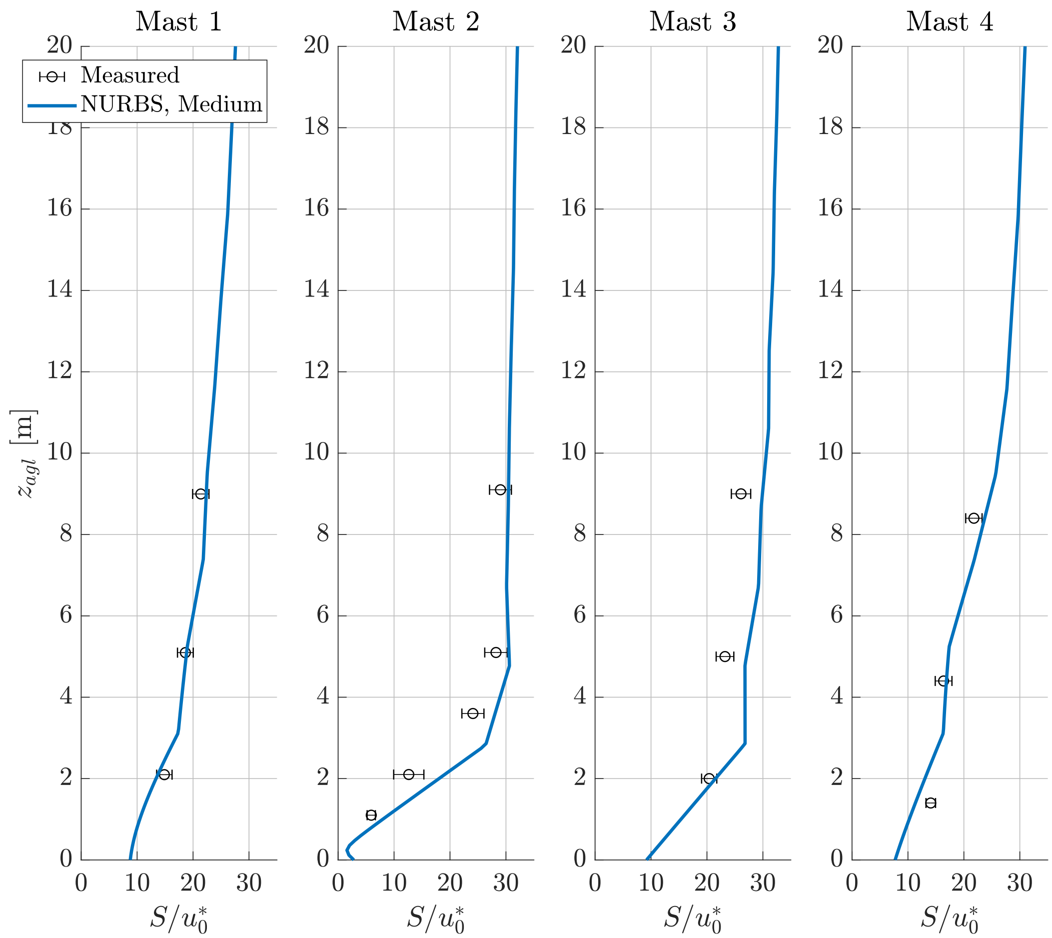

Figure 19: Mean velocity magnitude profiles comparing NURBS simulations with measured data

base of the hill on the downstream side, and mast 3 is located in the middle of the broad, nearly flat expanse on top of the hill. The simulations show very good match to the experimental data at masts 1 and 7, i.e. correctly capturing the velocity slowdown in front of the hill. Mast 2 and mast 5, located in recirculated regions just after the upstream slope and just after the downstream slope respectively, show slight over-prediction of the velocity close to the surface (below 5 m elevation). The simulations also show good agreement with the experimental measurements near the ground where velocity gradients are high, which is normally hard to capture with traditional discretization schemes.

Comparison of simulation results with measurements for the Bolund hill case is typically done in terms of velocity increase or decrease from an upstream reference location rather than in absolute values. Figure 21 plots the velocity speed-up along a horizontal line 5 m above the ground along the transect 'line B' (Figure 9). The velocity speed-up (non-dimensional increase in velocity

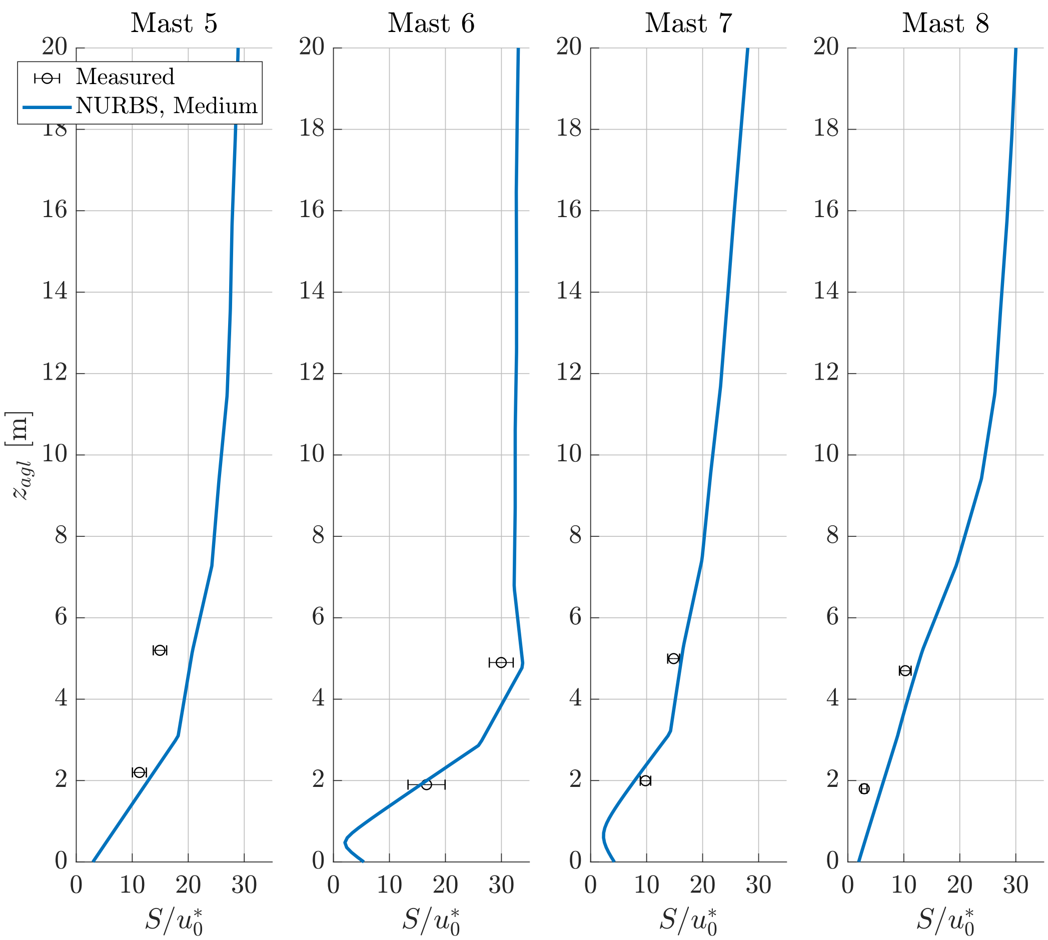

Figure 20: Mean velocity magnitude profiles comparing NURBS simulations with measured data

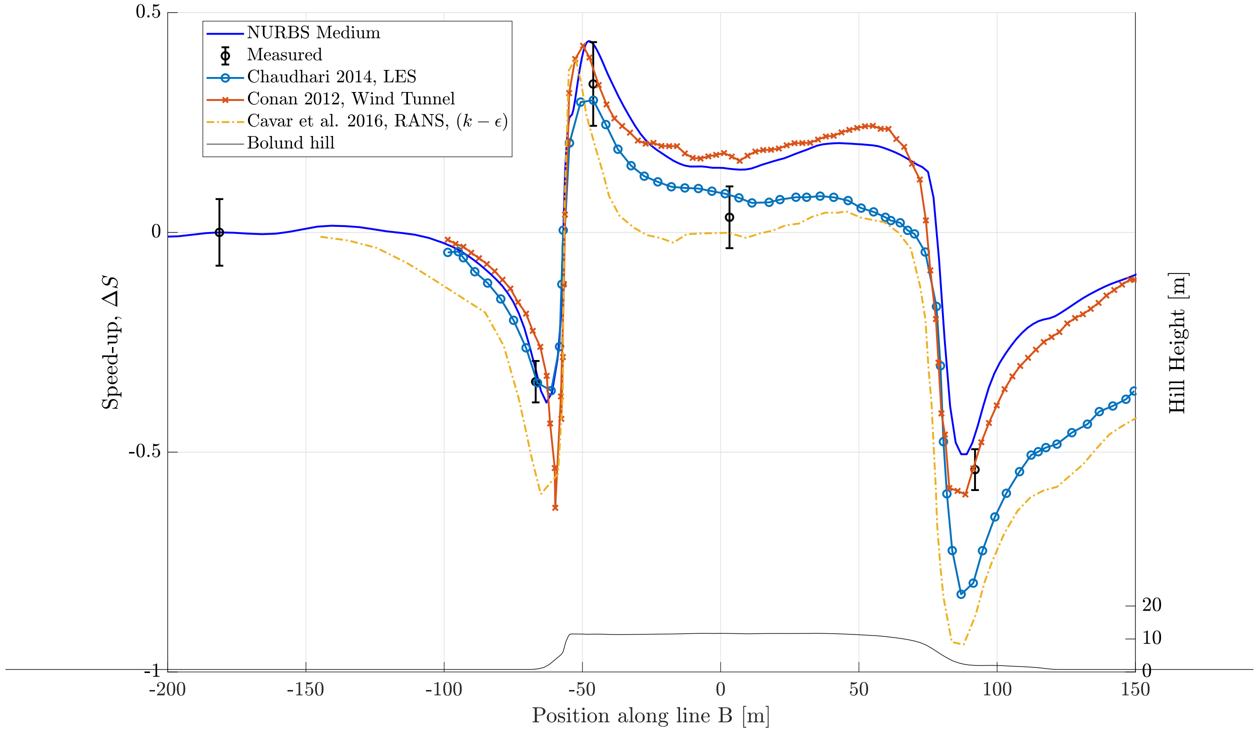

Figure 21: Velocity speed-up 5 m above ground level along line B

magnitude relative to the reference mast), defined as

$$\Delta S = \frac{\overline{s}_{z_{agl}} - \overline{s_0}_{z_{agl}}}{\overline{s_0}_{z_{agl}}} \tag{24}$$

where the over-bar indicates a time average and the reference velocity magnitude, s_0, is calculated 5 m above the ground at the location of Mast 0 (Figure 9) in the inflow region of the domain. The measured data points are shown with open circle markers and the terrain profile is plotted near the bottom of the figure with the elevation corresponding to the vertical axis on the right-hand side. The simulations accurately predict the velocity slowdown just in front of the hill, and are also within one standard deviation of the measured value at the tower just after the top of the hill. The simulations, however, slightly over-predict the velocity magnitude in the middle of the broad flat area on top of the hill. The velocity slowdown on the lee side of the hill is well captured. Results of previously published studies on Bolund hill are also plotted in Figure 21, including LES from Chaudhari [42], a wind tunnel experiment by Conan et al. [46], and RANS simulation from Cavar et al. [41]. The NURBS simulation shows an overall better match to the measured data when compared to those studies.

5. Conclusion and future work

Accurate prediction of local flow field in complex terrain is critical for many engineering applications, including wind energy, which require the development of a high-fidelity framework to model atmospheric flows over complex geographical terrain. In this paper we applied a variational multi-scale model to representative areas of complex terrain to establish such a framework. We adopted two special discretization techniques, linear finite elements and quadratic non-uniform rational B-splines (NURBS). We also highlighted the needs for special treatment of the no-slip boundary condition at the terrain surface. The weakly-enforced formulation of the no-slip boundary condition was used to relax grid resolution requirements near the wall. It consistently gave more accurate results on even coarser meshes when compared to a standard strong imposition approach. The model was validated against two well documented cases of airflow over complex terrain, the Gaussian and Bolund hills. We find that VMS formulation shows excellent agreement with published data for both cases, without the use of any *ah-hoc* turbulent eddy-viscosity models. The simulations with NURBS-based discretization showed better accuracy for the Gaussian hill even on a coarser meshes. Simulations using quadratic NURBS discretization was performed for the Bolund hill showing excellent agreement with the measured data. These results indicate the potential of the variational multi-scale formulation combined with a NURBS approach to predict airflow over complex terrain.

Future work will continue to examine cases of highly complex terrain such as the Perdigão location. The Perdigão location was recently the subject of a large scale field study, part of the New European Wind Atlas, to investigate flow in complex terrain, including the interaction of wind turbine wakes with the terrain. We will also perform numerical simulations using NURBS discretization for ABL flow with different stratification regimes, which has a significant impact on the flow behaviour over the terrain and especially when interacting with wind turbines. Finally, we will perform the simulation of the entire wind farm under the realistic turbulent, stratified inflow condition in a complex terrain.

Acknowledgments

M. Ravensbergen and A. Korobenko was partially supported by NSERC Discovery Grant, RGPIN-2017-03781. We thank Compute Canada and Advanced Research Computing (ARC) at the University of Calgary for providing HPC resources that have contributed to the research results reported in this paper.

References

[1] Akkerman, I., Bazilevs, Y., Benson, D. J., Farthing, M. W., Kees, C. E., 2012. Free-surface flow and fluid–object interaction modeling with emphasis on ship hydrodynamics. Journal of Applied Mechanics 79, 010905.

[2] Akkerman, I., Dunaway, J., Kvandal, J., Spinks, J., Bazilevs, Y., 2012. Toward free-surface modeling of planing vessels: simulation of the Fridsma hull using ALE-VMS. Computational Mechanics 50, 719–727.

[3] Apsley, D. D., Castro, I. P., 1997. Flow and dispersion over hills: Comparison between numerical predictions and experimental data. Journal of Wind Engineering and Industrial Aerodynamics 67-68, 375–386.

[4] Apsley, D. D., Castro, I. P., 1997. Numerical modelling of flow and dispersion around cinder cone butte. Atmospheric Environment 31 (7), 1059–1071.

[5] Augier, B., Yan, J., Korobenko, A., Czarnowski, J., Ketterman, G., Bazilevs, Y., 2015. Experimental and numerical FSI study of compliant hydrofoils. Computational Mechanics 55, 1079–1090.

[6] Ayotte, K. W., 2008. Computational modelling for wind energy assessment. Journal of Wind Engineering and Industrial Aerodynamics 96 (10-11), 1571–1590.

[7] Ayotte, K. W., Hughes, D. E., 2004. Observations of Boundary-Layer Wind-Tunnel Flow over Isolated Ridges of Varying Steepness and Roughness. Boundary-Layer Meteorology 112 (3), 525–556.

[8] Baba-Ahmadi, M. H., Tabor, G., 2009. Inlet conditions for LES using mapping and feedback control. Computers and Fluids 38 (6), 1299–1311.
URL http://dx.doi.org/10.1016/j.compfluid.2009.02.001

[9] Barnard, J., 1991. An evaluation of three models designed for siting wind turbines in areas of complex terrain. Solar Energy 46 (5), 283–294.
URL https://linkinghub.elsevier.com/retrieve/pii/0038092X9190096F

[10] Bayram, A., Bear, C., Bear, M., Korobenko, A., 2020. Performance analysis of two vertical-axis hydrokinetic turbines using variational multiscale method. Computers and Fluids 200, 104432, available online.

[11] Bayram, A., Korobenko, A., 2020. Variational multiscale framework for cavitating flows, *Computational Mechanics*, submitted.

[12] Bazilevs, Y., Calo, V. M., Cottrell, J. A., Hughes, T. J., Reali, A., Scovazzi, G., 2007.

Variational multiscale residual-based turbulence modeling for large eddy simulation of incompressible flows. Computer Methods in Applied Mechanics and Engineering 197 (1-4), 173–201.

[13] Bazilevs, Y., Calo, V. M., Hughes, T. J. R., Zhang, Y., 2008. Isogeometric fluid–structure interaction: theory, algorithms, and computations. Computational Mechanics 43, 3–37.

[14] Bazilevs, Y., Calo, V. M., Zhang, Y., Hughes, T. J. R., 2006. Isogeometric fluid–structure interaction analysis with applications to arterial blood flow. Computational Mechanics 38, 310–322.

[15] Bazilevs, Y., Gohean, J. R., Hughes, T. J. R., Moser, R. D., Zhang, Y., 2009. Patient-specific isogeometric fluid–structure interaction analysis of thoracic aortic blood flow due to implantation of the Jarvik 2000 left ventricular assist device. Computer Methods in Applied Mechanics and Engineering 198, 3534–3550.

[16] Bazilevs, Y., Hsu, M.-C., Akkerman, I., Wright, S., Takizawa, K., Henicke, B., Spielman, T., Tezduyar, T. E., 2011. 3D simulation of wind turbine rotors at full scale. Part I: Geometry modeling and aerodynamics. International Journal for Numerical Methods in Fluids 65, 207–235.

[17] Bazilevs, Y., Hsu, M.-C., Akkerman, I., Wright, S., Takizawa, K., Henicke, B., Spielman, T., Tezduyar, T. E., jan 2011. 3D simulation of wind turbine rotors at full scale. Part I: Geometry modeling and aerodynamics. International Journal for Numerical Methods in Fluids 65 (1-3), 207–235.
URL http://doi.wiley.com/10.1002/fld.2400

[18] Bazilevs, Y., Hsu, M.-C., Benson, D., Sankaran, S., Marsden, A., 2009. Computational fluid–structure interaction: Methods and application to a total cavopulmonary connection. Computational Mechanics 45, 77–89.

[19] Bazilevs, Y., Hsu, M.-C., Kiendl, J., Wüchner, R., Bletzinger, K.-U., 2011. 3D simulation of wind turbine rotors at full scale. Part II: Fluid–structure interaction modeling with composite blades. International Journal for Numerical Methods in Fluids 65, 236–253.

[20] Bazilevs, Y., Hsu, M.-C., Scott, M. A., 2012. Isogeometric fluid–structure interaction analysis with emphasis on non-matching discretizations, and with application to wind turbines. Computer Methods in Applied Mechanics and Engineering 249-252, 28–41.

[21] Bazilevs, Y., Hsu, M.-C., Zhang, Y., Wang, W., Kvamsdal, T., Hentschel, S., Isaksen, J., 2010. Computational fluid–structure interaction: Methods and application to cerebral aneurysms. Biomechanics and Modeling in Mechanobiology 9, 481–498.

[22] Bazilevs, Y., Hsu, M.-C., Zhang, Y., Wang, W., Liang, X., Kvamsdal, T., Brekken, R., Isaksen, J., 2010. A fully-coupled fluid–structure interaction simulation of cerebral aneurysms. Computational Mechanics 46, 3–16.

[23] Bazilevs, Y., Hughes, T. J. R., 2007. Weak imposition of Dirichlet boundary conditions in fluid mechanics. Computers and Fluids 36 (1), 12–26.

[24] Bazilevs, Y., Korobenko, A., Deng, X., Yan, J., 2015. Novel structural modeling and mesh moving techniques for advanced FSI simulation of wind turbines. International Journal for Numerical Methods in Engineering 102, 766–783.

[25] Bazilevs, Y., Korobenko, A., Deng, X., Yan, J., Kinzel, M., Dabiri, J. O., 2014. FSI modeling of vertical-axis wind turbines. Journal of Applied Mechanics 81, 081006.

[26] Bazilevs, Y., Korobenko, A., Yan, J., Pal, A., Gohari, S. M. I., Sarkar, S., 2015. ALE–VMS formulation for stratified turbulent incompressible flows with applications. Mathematical Models and Methods in Applied Sciences 25, 2349–2375.

[27] Bazilevs, Y., Michler, C., Calo, V. M., Hughes, T. J., 2007. Weak Dirichlet boundary conditions for wall-bounded turbulent flows. Computer Methods in Applied Mechanics and Engineering 196 (49-52), 4853–4862.

[28] Bazilevs, Y., Takizawa, K., Tezduyar, T. E., February 2013. Computational Fluid–Structure Interaction: Methods and Applications. Wiley.

[29] Bazilevs, Y., Takizawa, K., Tezduyar, T. E., Hsu, M.-C., Kostov, N., McIntyre, S., 2014. Aerodynamic and FSI analysis of wind turbines with the ALE-VMS and ST-VMS methods. Archives of Computational Methods in Engineering 21, 359–398.

[30] Bechmann, A., Berg, J., Courtney, M., Jorgensen, H., Mann, J., Sørensen, N., 2009. The Bolund Experiment : Overview and Background. Tech. Rep. July, Riso DTU National Laboratory for Sustainable Energy.

[31] Bechmann, A., Sørensen, N., Berg, J., Mann, J., Réthoré, P. E., 2011. The Bolund Experiment, Part II: Blind Comparison of Microscale Flow Models. Boundary-Layer Meteorology 141 (2), 245–271.

[32] Berg, J., Mann, J., Bechmann, A., Courtney, M. S., Jørgensen, H. E., 2011. The Bolund Experiment, Part I: Flow Over a Steep, Three-Dimensional Hill. Boundary-Layer Meteorology 141 (2), 219–243.

[33] Berg, J., Troldborg, N., Menke, R., Patton, E. G., Sullivan, P. P., Mann, J., Sørensen, N., jun 2018. Flow in complex terrain - a Large Eddy Simulation comparison study. Journal of

Physics: Conference Series 1037 (7), 072015.
URL http://stacks.iop.org/1742-6596/1037/i=7/a=072015?key=crossref.6a6cce084447b324ab2e48509a142bec

[34] Berg, J., Troldborg, N., Sørensen, N. N., Patton, E. G., Sullivan, P. P., 2017. Large-Eddy Simulation of turbine wake in complex terrain. Journal of Physics: Conference Series 854 (1), 12003.
URL http://stacks.iop.org/1742-6596/854/i=1/a=012003?key=crossref.7f4114769475b0030a8883dc6140c902

[35] Blocken, B., van der Hout, A., Dekker, J., Weiler, O., 2015. CFD simulation of wind flow over natural complex terrain: Case study with validation by field measurements for Ria de Ferrol, Galicia, Spain. Journal of Wind Engineering and Industrial Aerodynamics 147, 43–57.
URL http://dx.doi.org/10.1016/j.jweia.2015.09.007

[36] Bowen, A. J., Mortensen, N. G., 2004. WAsP prediction errors due to site orography. Tech. rep., Technical University of Denmark, DTU Wind Energy, Roskilde, Denmark.

[37] Bradley, E. F., 1980. An experimental study of the profiles of wind speed, shearing stress and turbulence at the crest of a large hill. Quarterly Journal of the Royal Meteorological Society 106 (447), 101–123.

[38] Britter, R. E., Hunt, J. C., Richards, K. J., 1981. Air flow over a twodimensional hill: Studies of velocity speedup, roughness effects and turbulence. Quarterly Journal of the Royal Meteorological Society 107 (451), 91–110.

[39] Cabezón Martínez, D., Hansen, K. S., Barthelmie, R. J., jan 2010. Analysis and validation of CFD wind farm models in complex terrain. Effects induced by topography and wind turbines. 2010 European Wind Energy Conference and Exhibition.

[40] Castro, F. A., Palma, J. M. L. M., Lopes, A. S., 2003. Simulation of the Askervein flow. Part 1: Reynolds averaged Navier-Stokes equations (k - ϵ turbulence model). Boundary-Layer Meteorology 107 (3), 501–530.

[41] Cavar, D., Réthoré, P.-E., Bechmann, A., Sørensen, N. N., Martinez, B., Zahle, F., Berg, J., Kelly, M. C., may 2016. Comparison of OpenFOAM and EllipSys3D for neutral atmospheric flow over complex terrain. Wind Energy Science 1 (1), 55–70.
URL http://www.wind-energ-sci-discuss.net/wes-2016-3/https://www.wind-energ-sci.net/1/55/2016/

[42] Chaudhari, A., 2014. Large-eddy simulation of wind flows over complex terrains for wind

energy applications. Ph.D. thesis, Lappeenranta University of Technology.
URL https://doria32-kk.lib.helsinki.fi/handle/10024/103100

[43] Cheng, Y., Lien, F. S., Yee, E., Sinclair, R., 2003. A comparison of large Eddy simulations with a standard k-?? Reynolds-averaged Navier-Stokes model for the prediction of a fully developed turbulent flow over a matrix of cubes. Journal of Wind Engineering and Industrial Aerodynamics 91 (11), 1301–1328.

[44] Churchfield, M. J., Lee, S., Moriarty, P. J., feb 2014. Adding complex terrain and stable atmospheric condition capability to the OpenFOAM-based flow solver of the simulator for on/offshore wind farm applications (SOWFA). ITM Web of Conferences 2 (September), 02001.
URL http://www.itm-conferences.org/10.1051/itmconf/20140202001

[45] Conan, B., Chaudhari, A., Aubrun, S., van Beeck, J., Hämäläinen, J., Hellsten, A., 2016. Experimental and Numerical Modelling of Flow over Complex Terrain: The Bolund Hill. Boundary-Layer Meteorology 158 (2), 183–208.

[46] Conan, B., van Beeck, J., Aubrun, S., 2012. Sand erosion technique applied to wind resource assessment. Journal of Wind Engineering and Industrial Aerodynamics 104-106, 322–329.
URL http://dx.doi.org/10.1016/j.jweia.2012.03.017

[47] Coppin, P. A., Bradley, E. F., Finnigan, J. J., 1994. Measurements of flow over an elongated ridge and its thermal stability dependence: The mean field. Boundary-Layer Meteorology 69 (1-2), 173–199.

[48] Dawson, P., Stock, D. E., Lamb, B., 1991. The Numerical Simulation of Airflow and Dispersion in Three-Dimensional Atmospheric Recirculation Zones. Journal of Applied Meteorology (1988-2005) 30 (7), 1005–1024.

[49] Dean, R. B., 1978. Reynolds number dependence of skin friction and other bulk flow variables in two-dimensional rectangular duct flow. Journal of Fluids Engineering 100 (June 1978), 215–223.

[50] El Kasmi, A., Masson, C., nov 2010. Turbulence modeling of atmospheric boundary layer flow over complex terrain: a comparison of models at wind tunnel and full scale. Wind Energy 13 (8), 689–704.
URL http://doi.wiley.com/10.1002/we.390

[51] Enger, L., 1990. Simulation of dispersion in moderately complex terrain-Part A. The fluid dynamic model. Atmospheric Environment Part A, General Topics 24 (9), 2431–2446.

[52] Enger, L., Koračin, D., 1995. Simulations of dispersion in complex terrain using a higher-

order closure model. Atmospheric Environment 29 (18), 2449–2465.

[53] Ferrante, A., Elghobashi, S., jul 2004. A robust method for generating inflow conditions for direct simulations of spatially-developing turbulent boundary layers. Journal of Computational Physics 198 (1), 372–387.
URL https://linkinghub.elsevier.com/retrieve/pii/S0021999104000348

[54] Fluids Engineering Division ASME, A., 2008. Procedure for Estimation and Reporting of Uncertainty Due to Discretization in CFD Applications. Journal of Fluids Engineering 130 (7), 078001.
URL http://fluidsengineering.asmedigitalcollection.asme.org/article.aspx?articleid=1434171

[55] Gomes Da Silva, A. F., Peña, A., Hahmann, A. N., Zaparoli, E. L., 2018. Evaluation of two microscale flow models through two wind climate generalization procedures using observations from seven masts at a complex site in Brazil. Journal of Renewable and Sustainable Energy 10 (5).

[56] Gong, W., Taylor, P. A., Dörnbrack, A., 1996. Turbulent boundary-layer flow over fixed aerodynamically rough two-dimensional sinusoidal waves. Journal of Fluid Mechanics 312, 1–37.

[57] Han, Y., Stoellinger, M., Naughton, J., sep 2016. Large eddy simulation for atmospheric boundary layer flow over flat and complex terrains. Journal of Physics: Conference Series 753 (3), 032044.
URL http://stacks.iop.org/1742-6596/753/i=3/a=032044?key=crossref.8b139dfc5780bf2584a62f37c5202bcd

[58] Helgedagsrud, T. A., Bazilevs, Y., Korobenko, A., Mathisen, K. M., Oiseth, O. A., 2018. Using ALE-VMS to compute aerodynamic derivatives of bridge sections. Computers and FluidsPublished online.

[59] Helgedagsrud, T. A., Bazilevs, Y., Mathisen, K. M., Oiseth, O. A., 2018. Computational and experimental investigation of free vibration and flutter of bridge decks. Computational MechanicsPublished online.

[60] Helgedagsrud, T. A., Bazilevs, Y., Mathisen, K. M., Yan, J., Øseth, O. A., may 2019. Modeling and simulation of bridge-section buffeting response in turbulent flow. Mathematical Models and Methods in Applied Sciences 29 (05), 939–966.
URL https://www.worldscientific.com/doi/abs/10.1142/S0218202519410045

[61] Hewer, F. E., 1998. Non-linear numerical model predictions of flow over an isolated hill of

moderate slope. Boundary-Layer Meteorology 87 (3), 381–408.

[62] Hsu, M.-C., Akkerman, I., Bazilevs, Y., 2011. High-performance computing of wind turbine aerodynamics using isogeometric analysis. Computers and Fluids 49, 93–100.

[63] Hsu, M.-C., Akkerman, I., Bazilevs, Y., 2014. Finite element simulation of wind turbine aerodynamics: Validation study using NREL Phase VI experiment. Wind Energy 17, 461–481.

[64] Hsu, M.-C., Bazilevs, Y., 2011. Blood vessel tissue prestress modeling for vascular fluid–structure interaction simulations. Finite Elements in Analysis and Design 47, 593–599.

[65] Hsu, M.-C., Kamensky, D., 2018. Immersogeometric Analysis of Bioprosthetic Heart Valves, Using the Dynamic Augmented Lagrangian Method. In: Frontiers in Computational Fluid–Structure Interaction and Flow Simulation. Springer International Publishing, Cham, pp. 167–212.

[66] Hsu, M.-C., Kamensky, D., Bazilevs, Y., Sacks, M. S., Hughes, T. J. R., 2014. Fluid–structure interaction analysis of bioprosthetic heart valves: significance of arterial wall deformation. Computational Mechanics 54, 1055–1071.

[67] Hsu, M.-C., Kamensky, D., Xu, F., Kiendl, J., Wang, C., Wu, M. C. H., Mineroff, J., Reali, A., Bazilevs, Y., Sacks, M. S., 2015. Dynamic and fluid–structure interaction simulations of bioprosthetic heart valves using parametric design with T-splines and Fung-type material models. Computational Mechanics 55, 1211–1225.

[68] Hughes, T. J., Cottrell, J. A., Bazilevs, Y., 2005. Isogeometric analysis: CAD, finite elements, NURBS, exact geometry and mesh refinement. Computer Methods in Applied Mechanics and Engineering 194 (39-41), 4135–4195.

[69] Hughes, T. J., Feijóo, G. R., Mazzei, L., Quincy, J.-B., 1998. The variational multiscale method-a paradigm for computational mechanics. Computer Methods in Applied Mechanics and Engineering 166 (1-2), 3–24.
URL http://linkinghub.elsevier.com/retrieve/pii/S0045782598000796

[70] Hughes, T. J. R., Mazzei, L., Jansen, K. E., 2000. Large Eddy Simulation and the variational multiscale method. Computing and Visualization in Science 3, 47–59.

[71] Jackson, P. S., Hunt, J. C. R., oct 1975. Turbulent wind flow over a low hill. Quarterly Journal of the Royal Meteorological Society 101 (430), 929–955.
URL http://doi.wiley.com/10.1002/qj.49710143015

[72] Jenkins, G., Mason, P., Moores, W., Sykes, R., oct 1981. Measurements of the flow structure

around Ailsa Craig, a steep, three-dimensional, isolated hill. Quarterly Journal of the Royal Meteorological Society 107 (454), 833–851.
URL http://www.ingentaselect.com/rpsv/cgi-bin/cgi?ini=xref{&}body=linker{&}reqdoi=10.1256/smsqj.45405

[73] Johnson, C., 1987. Numerical solution of partial differential equations by the finite element method. Cambridge University Press, Sweden.

[74] Kamensky, D., Evans, J. A., Hsu, M.-C., Bazilevs, Y., 2017. Projection-based stabilization of interface Lagrange multipliers in immersogeometric fluid–thin structure interaction analysis, with application to heart valve modeling. Computers and Mathematics with Applications 74 (9), 2068–2088.

[75] Kamensky, D., Hsu, M.-C., Schillinger, D., Evans, J. A., Aggarwal, A., Bazilevs, Y., Sacks, M. S., Hughes, T. J. R., 2015. An immersogeometric variational framework for fluid-structure interaction: Application to bioprosthetic heart valves. Computer Methods in Applied Mechanics and Engineering 284, 1005–1053.

[76] Kamensky, D., Xu, F., Lee, C.-H., Yan, J., Bazilevs, Y., Hsu, M.-C., 2018. A contact formulation based on a volumetric potential: Application to isogeometric simulations of atrioventricular valves. Computer Methods in Applied Mechanics and Engineering 330, 522–546.

[77] Kanai, T., Takizawa, K., Tezduyar, T. E., Tanaka, T., Hartmann, A., 2019. Compressible-flow geometric-porosity modeling and spacecraft parachute computation with isogeometric discretization. Computational Mechanics 63, 301–321.

[78] Khurshudyan, L. H., Snyder, W. H., Nekrasov, I. V., 1981. Flow and dispersion of pollutants over 2-dimensional hills. Tech. Rep. EPA-600/4-81-067, U.S. Environmental Protection Agency.

[79] Kim, H. G., Patel, V. C., Lee, C. M., 2000. Numerical simulation of wind flow over hilly terrain. Journal of Wind Engineering and Industrial Aerodynamics 87 (1), 45–60.

[80] Kirkil, G., Mirocha, J., Bou-Zeid, E., Chow, F. K., Kosović, B., 2012. Implementation and Evaluation of Dynamic Subfilter-Scale Stress Models for Large-Eddy Simulation Using WRF*. Monthly Weather Review 140 (1), 266–284.

[81] Korobenko, A., Bazilevs, Y., Takizawa, K., Tezduyar, T. E., 2018. Recent advances in ALE-VMS and ST-VMS computational aerodynamic and FSI analysis of wind turbines. In: Tezduyar, T. E. (Ed.), Frontiers in Computational Fluid–Structure Interaction and Flow Simulation: Research from Lead Investigators under Forty – 2018. Modeling and Simulation in Science, Engineering and Technology. Springer, pp. 253–336.

[82] Korobenko, A., Bazilevs, Y., Takizawa, K., Tezduyar, T. E., 2019. Computer modeling of wind turbines: 1. ALE-VMS and ST-VMS aerodynamic and FSI analysis. Archives of Computational Methods in Engineering 26, 1059–1099.

[83] Korobenko, A., Hsu, M.-C., Akkerman, I., Bazilevs, Y., 2013. Aerodynamic simulation of vertical-axis wind turbines. Journal of Applied Mechanics 81, 021011.

[84] Korobenko, A., Hsu, M.-C., Akkerman, I., Tippmann, J., Bazilevs, Y., 2013. Structural mechanics modeling and FSI simulation of wind turbines. Mathematical Models and Methods in Applied Sciences 23, 249–272.

[85] Korobenko, A., Yan, J., Gohari, S. M. I., Sarkar, S., Bazilevs, Y., 2017. FSI simulation of two back-to-back wind turbines in atmospheric boundary layer flow. Computers & Fluids 158, 167–175.

[86] Kuraishi, T., Takizawa, K., Tezduyar, T. E., 2018. Space–time computational analysis of tire aerodynamics with actual geometry, road contact and tire deformation. In: Tezduyar, T. E. (Ed.), Frontiers in Computational Fluid–Structure Interaction and Flow Simulation: Research from Lead Investigators under Forty – 2018. Modeling and Simulation in Science, Engineering and Technology. Springer, pp. 337–376.

[87] Kuraishi, T., Takizawa, K., Tezduyar, T. E., 2019. Tire aerodynamics with actual tire geometry, road contact and tire deformation. Computational Mechanics 63, 1165–1185.

[88] Kuraishi, T., Takizawa, K., Tezduyar, T. E., July 2019. Space–time computational analysis of tire aerodynamics with actual geometry, road contact, tire deformation, road roughness and fluid film, Computational Mechanics, published online, DOI: 10.1007/s00466-019-01746-8.

[89] Lavery, T., Bass, A., Strimaitis, D., Venkatram, A., Green, B., 1981. EPA complex terrain model development: first milestone report 1981. Tech. rep., United States Environmental Protection Agency, Washington, D.C., EPA/600/3-82/036.

[90] Lee, C.-H., Laurence, D. W., Ross, C. J., Kramer, K. E., Babu, A. R., Johnson, E. L., Hsu, M.-C., Aggarwal, A., Mir, A., Burkhart, H. M., Towner, R. A., Baumwart, R., Wu, Y., 2019. Mechanics of the Tricuspid Valve—From Clinical Diagnosis/Treatment, In-Vivo and In-Vitro Investigations, to Patient-Specific Biomechanical Modeling. Bioengineering 6 (2), 47–40.

[91] Li, C., Zhou, S., Xiao, Y., Huang, Q., Li, L., Chan, P. W., aug 2017. Effects of inflow conditions on mountainous/urban wind environment simulation. Building Simulation 10 (4), 573–588.

URL http://link.springer.com/10.1007/s12273-017-0348-1

[92] Long, C. C., Esmaily-Moghadam, M., Marsden, A. L., Bazilevs, Y., 2014. Computation of residence time in the simulation of pulsatile ventricular assist devices. Computational Mechanics 54, 911–919.

[93] Long, C. C., Marsden, A. L., Bazilevs, Y., 2013. Fluid–structure interaction simulation of pulsatile ventricular assist devices. Computational Mechanics 52, 971–981.

[94] Long, C. C., Marsden, A. L., Bazilevs, Y., 2014. Shape optimization of pulsatile ventricular assist devices using FSI to minimize thrombotic risk. Computational Mechanics 54, 921–932.

[95] Lund, T. S., Wu, X., Squires, K. D., mar 1998. Generation of Turbulent Inflow Data for Spatially-Developing Boundary Layer Simulations. Journal of Computational Physics 140 (2), 233–258.
URL https://linkinghub.elsevier.com/retrieve/pii/S002199919895882X

[96] Makridis, A., 2012. Modelling of wind turbine wakes in complex terrain using Computational Fluid Dynamics. Ph.D. thesis, University of Edinburgh.

[97] Mann, J., Angelou, N., Arnqvist, J., Callies, D., Cantero, E., Arroyo, R. C., Courtney, M., Cuxart, J., Dellwik, E., Gottschall, J., Ivanell, S., Kühn, P., Lea, G., Matos, J. C., Palma, J. M. L. M., Pauscher, L., Peña, A., Rodrigo, J. S., Söderberg, S., Vasiljevic, N., Rodrigues, C. V., apr 2017. Complex terrain experiments in the New European Wind Atlas. Philosophical Transactions of the Royal Society A: Mathematical, Physical and Engineering Sciences 375 (2091), 20160101.
URL http://dx.doi.org/10.1098/rsta.2016.0101https://royalsocietypublishing.org/doi/10.1098/rsta.2016.0101

[98] Mason, P. J., King, J. C., 1985. Measurements and predictions of flow and turbulence over an isolated hill of moderate slope. The Quarterly Journal of the Royal Meteorological Society 111 (464), 617–640.

[99] Moser, R. D., Kim, J., Mansour, N. N., 1999. Direct numerical simulation of turbulent channel flow up to Reτ=590. Physics of Fluids 11 (4), 943–945.

[100] Munters, W., Meneveau, C., Meyers, J., 2016. Turbulent Inflow Precursor Method with Time-Varying Direction for Large-Eddy Simulations and Applications to Wind Farms. Boundary-Layer Meteorology 159 (2), 305–328.

[101] Ohba, R., Hara, T., Nakamura, S., Ohya, Y., Uchida, T., 2002. Gas diffusion over an isolated hill under neutral, stable and unstable conditions. Atmospheric Environment 36 (36-37),

5697–5707.

[102] Otoguro, Y., Takizawa, K., Tezduyar, T. E., 2017. Space–time VMS computational flow analysis with isogeometric discretization and a general-purpose NURBS mesh generation method. Computers & Fluids 158, 189–200.

[103] Otoguro, Y., Takizawa, K., Tezduyar, T. E., 2018. A general-purpose NURBS mesh generation method for complex geometries. In: Tezduyar, T. E. (Ed.), Frontiers in Computational Fluid–Structure Interaction and Flow Simulation: Research from Lead Investigators under Forty – 2018. Modeling and Simulation in Science, Engineering and Technology. Springer, pp. 399–434.

[104] Otoguro, Y., Takizawa, K., Tezduyar, T. E., Nagaoka, K., Avsar, R., Zhang, Y., 2019. Space–time VMS flow analysis of a turbocharger turbine with isogeometric discretization: Computations with time-dependent and steady-inflow representations of the intake/exhaust cycle. Computational Mechanics 64, 1403–1419.

[105] Otoguro, Y., Takizawa, K., Tezduyar, T. E., Nagaoka, K., Mei, S., 2019. Turbocharger turbine and exhaust manifold flow computation with the Space–Time Variational Multiscale Method and Isogeometric Analysis. Computers & Fluids 179, 764–776.

[106] Paiva, L. M., Bodstein, G. C., Menezes, W. F., 2009. Numerical simulation of atmospheric boundary layer flow over isolated and vegetated hills using RAMS. Journal of Wind Engineering and Industrial Aerodynamics 97 (9-10), 439–454.
URL http://dx.doi.org/10.1016/j.jweia.2009.07.006

[107] Palma, J. M. L. M., Castro, F. A., Ribeiro, L. F., Rodrigues, A. H., Pinto, A. P., 2008. Linear and nonlinear models in wind resource assessment and wind turbine micro-siting in complex terrain. Journal of Wind Engineering and Industrial Aerodynamics 96 (12), 2308–2326.
URL http://linkinghub.elsevier.com/retrieve/pii/S0167610508001037

[108] Peralta, C., Parente, A., Balogh, M., Benocci, C., jun 2014. RANS simulation of the atmospheric boundary layer over complex terrain with a consistent k-epsilon model. In: 6th International Sympsium on Computational Wind Engineering.
URL https://linkinghub.elsevier.com/retrieve/pii/S0022231313000331

[109] Prospathopoulos, J., Politis, E. S., 2008. Evaluating Wake Models for Use in Complex Terrain. Centre for Renewable Energy Sources, 83–136.

[110] Prospathopoulos, J. M., Politis, E. S., Chaviaropoulos, P. K., 2012. Application of a 3D RANS solver on the complex hill of Bolund and assessment of the wind flow predictions. Journal of Wind Engineering and Industrial Aerodynamics 107-108, 149–159.

URL http://dx.doi.org/10.1016/j.jweia.2012.04.011

[111] Rasouli, A., Hangan, H., 2013. Microscale Computational Fluid Dynamics Simulation for Wind Mapping Over Complex Topographic Terrains. Journal of Solar Energy Engineering 135 (4), 041005.

[112] Ravensbergen, M., Bayram, A., Korobenko, A., 2020. Performance analysis of two vertical-axis hydrokinetic turbines using variational multiscale method. Computers and Fluids 200, 104465, available online.

[113] Ryan, W., Lamb, B., Robinson, E., jan 1984. An atmospheric tracer investigation of transport and diffusion around a large, isolated hill. Atmospheric Environment (1967) 18 (10), 2003–2021.
URL https://linkinghub.elsevier.com/retrieve/pii/0004698184901860

[114] Saad, Y., 2000. Iterative methods for sparse linear systems, 2nd Edition. Vol. 2. SIAM, Philadelphia, PA.
URL http://ieeexplore.ieee.org/lpdocs/epic03/wrapper.htm?arnumber=1231631{%}5Cnhttp://www.stanford.edu/class/cme324/saad.pdfhttp://books.google.com/books?id=ZdLeBlqYeF8C{&}printsec=frontcover{%}5Cnpapers2://publication/uuid/8B2FDD23-9886-4AFA-82EC-0F7C346B9AA7

[115] Sharma, P. K., Warudkar, V., Ahmed, S., oct 2018. Numerical and experimental analysis of the flow over sinusoidal hills. International Journal of Ambient Energy.
URL https://www.tandfonline.com/doi/full/10.1080/01430750.2018.1542622

[116] Silva Lopes, A., Palma, J. M., Castro, F. A., 2007. Simulation of the Askervein flow. Part 2: Large-eddy simulations. Boundary-Layer Meteorology 125 (1), 85–108.

[117] Spalding, D. B., 1961. A single formula for the "law of the wall". Journal of Applied Mechanics 7 (12), 3078.
URL http://arxiv.org/abs/cond-mat/9507132

[118] Stevens, R. J., Gayme, D. F., Meneveau, C., 2014. Large eddy simulation studies of the effects of alignment and wind farm length. Journal of Renewable and Sustainable Energy 6 (2).

[119] Suito, H., Takizawa, K., Huynh, V. Q. H., Sze, D., Ueda, T., 2014. FSI analysis of the blood flow and geometrical characteristics in the thoracic aorta. Computational Mechanics 54, 1035–1045.

[120] Suito, H., Takizawa, K., Huynh, V. Q. H., Sze, D., Ueda, T., Tezduyar, T. E., 2016. A geometrical-characteristics study in patient-specific FSI analysis of blood flow in the

thoracic aorta. In: Bazilevs, Y., Takizawa, K. (Eds.), Advances in Computational Fluid–Structure Interaction and Flow Simulation: New Methods and Challenging Computations. Modeling and Simulation in Science, Engineering and Technology. Springer, pp. 379–386.

[121] Sullivan, P. P., Patton, E. G., Ayotte, K. W., 2010. Turbulent flow over and around sinusoidal bumps, hills, gaps and craters derived from large eddy simulations. In: 19th Conference on Boundary Layer and Turbulence. p. Paper 1B.5.

[122] Tabor, G. R., Baba-Ahmadi, M. H., 2010. Inlet conditions for large eddy simulation: A review. Computers and Fluids 39 (4), 553–567.
URL http://dx.doi.org/10.1016/j.compfluid.2009.10.007

[123] Takizawa, K., 2014. Computational engineering analysis with the new-generation space–time methods. Computational Mechanics 54, 193–211.

[124] Takizawa, K., Bazilevs, Y., Tezduyar, T. E., Hsu, M.-C., 2019. Computational cardiovascular flow analysis with the variational multiscale methods. Journal of Advanced Engineering and Computation 3, 366–405.

[125] Takizawa, K., Bazilevs, Y., Tezduyar, T. E., Hsu, M.-C., Øiseth, O., Mathisen, K. M., Kostov, N., McIntyre, S., 2014. Engineering analysis and design with ALE-VMS and space–time methods. Archives of Computational Methods in Engineering 21, 481–508.

[126] Takizawa, K., Bazilevs, Y., Tezduyar, T. E., Long, C. C., Marsden, A. L., Schjodt, K., 2014. ST and ALE-VMS methods for patient-specific cardiovascular fluid mechanics modeling. Mathematical Models and Methods in Applied Sciences 24, 2437–2486.

[127] Takizawa, K., Henicke, B., Puntel, A., Kostov, N., Tezduyar, T. E., 2012. Space–time techniques for computational aerodynamics modeling of flapping wings of an actual locust. Computational Mechanics 50, 743–760.

[128] Takizawa, K., Henicke, B., Puntel, A., Kostov, N., Tezduyar, T. E., 2013. Computer modeling techniques for flapping-wing aerodynamics of a locust. Computers & Fluids 85, 125–134.

[129] Takizawa, K., Henicke, B., Puntel, A., Spielman, T., Tezduyar, T. E., 2012. Space–time computational techniques for the aerodynamics of flapping wings. Journal of Applied Mechanics 79, 010903.

[130] Takizawa, K., Kostov, N., Puntel, A., Henicke, B., Tezduyar, T. E., 2012. Space–time computational analysis of bio-inspired flapping-wing aerodynamics of a micro aerial vehicle. Computational Mechanics 50, 761–778.

[131] Takizawa, K., Montes, D., Fritze, M., McIntyre, S., Boben, J., Tezduyar, T. E., 2013. Methods for FSI modeling of spacecraft parachute dynamics and cover separation. Mathematical Models and Methods in Applied Sciences 23, 307–338.

[132] Takizawa, K., Montes, D., McIntyre, S., Tezduyar, T. E., 2013. Space–time VMS methods for modeling of incompressible flows at high Reynolds numbers. Mathematical Models and Methods in Applied Sciences 23, 223–248.

[133] Takizawa, K., Schjodt, K., Puntel, A., Kostov, N., Tezduyar, T. E., 2012. Patient-specific computer modeling of blood flow in cerebral arteries with aneurysm and stent. Computational Mechanics 50, 675–686.

[134] Takizawa, K., Schjodt, K., Puntel, A., Kostov, N., Tezduyar, T. E., 2013. Patient-specific computational analysis of the influence of a stent on the unsteady flow in cerebral aneurysms. Computational Mechanics 51, 1061–1073.

[135] Takizawa, K., Tezduyar, T. E., 2016. New directions in space–time computational methods. In: Bazilevs, Y., Takizawa, K. (Eds.), Advances in Computational Fluid–Structure Interaction and Flow Simulation: New Methods and Challenging Computations. Modeling and Simulation in Science, Engineering and Technology. Springer, pp. 159–178.

[136] Takizawa, K., Tezduyar, T. E., Asada, S., Kuraishi, T., 2016. Space–time method for flow computations with slip interfaces and topology changes (ST-SI-TC). Computers & Fluids 141, 124–134.

[137] Takizawa, K., Tezduyar, T. E., Buscher, A., 2015. Space–time computational analysis of MAV flapping-wing aerodynamics with wing clapping. Computational Mechanics 55, 1131–1141.

[138] Takizawa, K., Tezduyar, T. E., Buscher, A., Asada, S., 2014. Space–time fluid mechanics computation of heart valve models. Computational Mechanics 54, 973–986.

[139] Takizawa, K., Tezduyar, T. E., Buscher, A., Asada, S., 2014. Space–time interface-tracking with topology change (ST-TC). Computational Mechanics 54, 955–971.

[140] Takizawa, K., Tezduyar, T. E., Kanai, T., 2017. Porosity models and computational methods for compressible-flow aerodynamics of parachutes with geometric porosity. Mathematical Models and Methods in Applied Sciences 27, 771–806.

[141] Takizawa, K., Tezduyar, T. E., Kostov, N., 2014. Sequentially-coupled space–time FSI analysis of bio-inspired flapping-wing aerodynamics of an MAV. Computational Mechanics 54, 213–233.

[142] Takizawa, K., Tezduyar, T. E., Kuraishi, T., 2015. Multiscale ST methods for thermo-fluid analysis of a ground vehicle and its tires. Mathematical Models and Methods in Applied Sciences 25, 2227–2255.

[143] Takizawa, K., Tezduyar, T. E., Kuraishi, T., Tabata, S., Takagi, H., 2016. Computational thermo-fluid analysis of a disk brake. Computational Mechanics 57, 965–977.

[144] Takizawa, K., Tezduyar, T. E., McIntyre, S., Kostov, N., Kolesar, R., Habluetzel, C., 2014. Space–time VMS computation of wind-turbine rotor and tower aerodynamics. Computational Mechanics 53, 1–15.

[145] Takizawa, K., Tezduyar, T. E., Mochizuki, H., Hattori, H., Mei, S., Pan, L., Montel, K., 2015. Space–time VMS method for flow computations with slip interfaces (ST-SI). Mathematical Models and Methods in Applied Sciences 25, 2377–2406.

[146] Takizawa, K., Tezduyar, T. E., Otoguro, Y., Terahara, T., Kuraishi, T., Hattori, H., 2017. Turbocharger flow computations with the Space–Time Isogeometric Analysis (ST-IGA). Computers & Fluids 142, 15–20.

[147] Takizawa, K., Tezduyar, T. E., Terahara, T., 2016. Ram-air parachute structural and fluid mechanics computations with the space–time isogeometric analysis (ST-IGA). Computers & Fluids 141, 191–200.

[148] Takizawa, K., Tezduyar, T. E., Terahara, T., Sasaki, T., 2017. Heart valve flow computation with the integrated Space–Time VMS, Slip Interface, Topology Change and Isogeometric Discretization methods. Computers & Fluids 158, 176–188.

[149] Takizawa, K., Tezduyar, T. E., Terahara, T., Sasaki, T., 2018. Heart valve flow computation with the Space–Time Slip Interface Topology Change (ST-SI-TC) method and Isogeometric Analysis (IGA). In: Wriggers, P., Lenarz, T. (Eds.), Biomedical Technology: Modeling, Experiments and Simulation. Lecture Notes in Applied and Computational Mechanics. Springer, pp. 77–99.

[150] Takizawa, K., Tezduyar, T. E., Uchikawa, H., Terahara, T., Sasaki, T., Shiozaki, K., Yoshida, A., Komiya, K., Inoue, G., 2018. Aorta flow analysis and heart valve flow and structure analysis. In: Tezduyar, T. E. (Ed.), Frontiers in Computational Fluid–Structure Interaction and Flow Simulation: Research from Lead Investigators under Forty – 2018. Modeling and Simulation in Science, Engineering and Technology. Springer, pp. 29–89.

[151] Takizawa, K., Tezduyar, T. E., Uchikawa, H., Terahara, T., Sasaki, T., Yoshida, A., 2019. Mesh refinement influence and cardiac-cycle flow periodicity in aorta flow analysis with isogeometric discretization. Computers & Fluids 179, 790–798.

[152] Taylor, P., Lee, R., 1984. Simple guidelines for estimating wind speed variations due to small scale topographic features. Climatological Bulletin 18 (2), 3–32.

[153] Taylor, P. A., Mason, P. J., Bradley, E. F., 1987. Boundary-layer flow over low hills. Boundary-Layer Meteorology 39 (1-2), 107–132.

[154] Taylor, P. A., Walmsley, J. L., Salmon, J. R., 1983. A simple model of neutrally stratified boundary-layer flow over real terrain incorporating wavenumber-dependent scaling. Boundary-Layer Meteorology 26 (2), 169–189.

[155] Temel, O., Bricteux, L., van Beeck, J., mar 2018. Coupled WRF-OpenFOAM study of wind flow over complex terrain. Journal of Wind Engineering and Industrial Aerodynamics 174 (November 2017), 152–169.
URL https://doi.org/10.1016/j.jweia.2018.01.002https://linkinghub.elsevier.com/retrieve/pii/S0167610517308851

[156] Teunissen, H. W., Shokr, M. E., Bowen, A. J., Wood, C. J., Green, D. W., 1987. The Askervein Hill Project: Wind-tunnel simulations at three length scales. Boundary-Layer Meteorology 40 (1-2), 1–29.

[157] Tezduyar, T. E., oct 2003. Computation of moving boundaries and interfaces and stabilization parameters. International Journal for Numerical Methods in Fluids 43 (5), 555–575.
URL http://doi.wiley.com/10.1002/fld.505

[158] Tian, W., Ozbay, A., Hu, H., 2015. Terrain Effects on Characteristics of Surface Wind and Wind Turbine Wakes. Vol. 126. Elsevier B.V.
URL http://dx.doi.org/10.1016/j.proeng.2015.11.302

[159] Troen, I., Lundtang Petersen, E., 1989. European Wind Atlas. Ris{\o} National Laboratory.
URL http://orbit.dtu.dk/en/publications/european-wind-atlas(335e86f2-6d21-4191-8304-0b0a105089be).html

[160] Wan, F., Porté-Agel, F., Stoll, R., apr 2007. Evaluation of dynamic subgrid-scale models in large-eddy simulations of neutral turbulent flow over a two-dimensional sinusoidal hill. Atmospheric Environment 41 (13), 2719–2728.
URL https://linkinghub.elsevier.com/retrieve/pii/S1352231006011940

[161] Wang, C., Wu, M. C. H., Xu, F., Hsu, M.-C., Bazilevs, Y., 2017. Modeling of a hydraulic arresting gear using fluid–structure interaction and isogeometric analysis. Computers and Fluids 142, 3–14.

[162] Wood, N., aug 2000. Wind Flow Over Complex Terrain: A Historical Perspective and the Prospect for Large-Eddy Modelling. Boundary-Layer Meteorology 96 (1-2), 11–32.

URL http://link.springer.com/10.1023/A:1002017732694

[163] Wu, M. C. H., Kamensky, D., Wang, C., Herrema, A. J., Xu, F., Pigazzini, M. S., Verma, A., Marsden, A. L., Bazilevs, Y., Hsu, M.-C., 2017. Optimizing fluid–structure interaction systems with immersogeometric analysis and surrogate modeling: Application to a hydraulic arresting gear. Computer Methods in Applied Mechanics and Engineering 316, 668–693.

[164] Wu, M. C. H., Muchowski, H. M., Johnson, E. L., Rajanna, M. R., Hsu, M.-C., 2019. Immersogeometric fluid–structure interaction modeling and simulation of transcatheter aortic valve replacement. Computer Methods in Applied Mechanics and Engineering 357, 112556.

[165] Wu, M. C. H., Zakerzadeh, R., Kamensky, D., Kiendl, J., Sacks, M. S., Hsu, M.-C., 2018. An anisotropic constitutive model for immersogeometric fluid–structure interaction analysis of bioprosthetic heart valves. Journal of Biomechanics 74, 23–31.

[166] Xu, F., Bazilevs, Y., Hsu, M.-C., 2019. Immersogeometric analysis of compressible flows with application to aerodynamic simulation of rotorcraft. Mathematical Models and Methods in Applied Sciences 29 (05), 905–938.

[167] Xu, F., Morganti, S., Zakerzadeh, R., Kamensky, D., Auricchio, F., Reali, A., Hughes, T. J. R., Sacks, M. S., Hsu, M.-C., 2018. A framework for designing patient-specific bioprosthetic heart valves using immersogeometric fluid–structure interaction analysis. International Journal for Numerical Methods in Biomedical Engineering 34 (4), e2938.

[168] Xu, S., Gao, B., Hsu, M.-C., Ganapathysubramanian, B., 2019. A residual-based variational multiscale method with weak imposition of boundary conditions for buoyancy-driven flows. Computer Methods in Applied Mechanics and Engineering 352, 345–368.

[169] Xu, S., Liu, N., Yan, J., 2019. Residual-based variational multi-scale modeling for particle-laden gravity currents over flat and triangular wavy terrains. Computers and Fluids 188, 114–124.

[170] Xu, S., Xu, F., Kommajosula, A., Hsu, M.-C., Ganapathysubramanian, B., 2019. Immersogeometric analysis of moving objects in incompressible flows. Computers & Fluids 189, 24–33.

[171] Yan, J., Augier, B., Korobenko, A., Czarnowski, J., Ketterman, G., Bazilevs, Y., 2016. FSI modeling of a propulsion system based on compliant hydrofoils in a tandem configuration. Computers and Fluids 141, 201–211.

[172] Yan, J., Deng, X., Korobenko, A., Bazilevs, Y., 2017. Free-surface flow modeling and simulation of horizontal-axis tidal-stream turbines. Computers and Fluids 158, 157–166.

[173] Yan, J., Korobenko, A., Deng, X., Bazilevs, Y., 2016. Computational free-surface fluid–structure interaction with application to floating offshore wind turbines. Computers and Fluids 141, 155–174.

[174] Yan, J., Korobenko, A., Tejada-Martinez, A., Golshan, R., Bazilevs, Y., 2017. A new variational multiscale formulation for stratified incompressible turbulent flows. Computers and Fluids 158, 150–156.

[175] Yu, Y., Zhang, Y. J., Takizawa, K., Tezduyar, T. E., Sasaki, T., October 2019. Anatomically realistic lumen motion representation in patient-specific space–time isogeometric flow analysis of coronary arteries with time-dependent medical-image data, Computational Mechanics, published online, DOI: 10.1007/s00466-019-01774-4.

[176] Zakerzadeh, R., Hsu, M.-C., Sacks, M. S., 2017. Computational methods for the aortic heart valve and its replacements. Expert Review of Medical Devices 14 (11), 849–866.

[177] Zheng, K., Tian, W., Qin, J., Hu, H., jun 2017. Investigation of Wind Turbine Wakes over Complex Terrain Based on Actuator Disk Method. In: 35th AIAA Applied Aerodynamics Conference. Reston, Virginia.
URL https://arc.aiaa.org/doi/10.2514/6.2017-4073

[178] Zhu, Q., Yan, J., 2019. A moving-domain cfd solver in fenics with applications to tidal turbine simulations in turbulent flows. Computers and Mathematics with ApplicationsAccepted for publication.